Evolution of the thermal and dehydration state of sediments entering the North Sumatra Subduction Zone

Duncan E. Stevens[1*], Timothy J. Henstock[1], Lisa C. McNeill[1]

[1]School of Ocean and Earth Science, National Oceanography Centre Southampton, University of Southampton, Southampton, S014 3ZH, United Kingdom

Key Points

- Thermal modelling suggests diagenetic dehydration transformations are complete within the basal sediments prior to subduction/accretion
- The dehydration fluid source from basal sediments is theoretically large enough to generate a pre-décollement reflection polarity reversal
- Décollement depth at the deformation front may be driven by the interplay between lithology, hydrology, and temperature driven sediment dehydration and cementation

Abstract

Shallow slip on the plate-boundary fault during the 2004 Mw 9.2 Aceh-Andaman Earthquake, offshore North Sumatra, has been linked to thick incoming sediments on the oceanic plate with advanced diagenetic and sediment property changes at the depths of plate boundary fault development. We couple age control, physical and thermal property measurements from International Ocean Discovery Program (IODP) drilling with multichannel seismic reflection data to reconstruct the thermal structure and evolution of the incoming sediment column, up to the point of accretion/subduction. Lithospheric thermal rejuvenation around 58 Ma is required to explain anomalously high heat flux at IODP Site U1480, and heat flux within the trench is suppressed by very high sediment accumulation rates during development of a thick trench wedge. Accumulation of up to ~4.5 km of thick Nicobar Fan and trench wedge sediments produces temperatures >150 °C within the basal sediments where the décollement develops, resulting in total pre-subduction diagenetic dehydration of basal sediments. The smectite-illite transformation within these basal sediments produces sufficient fluid to explain a polarity reversal on a pre-décollement reflector. We suggest that the boundary between basal-pelagic and siliclastic-fan sediments has trapped fluid over the last ~1 Myr, as a result of primary lithological properties,

diagenetic fluid release and cementation, controlling décollement formation at this weakened level. Pre-subduction dehydration of large portions of the accreted sediment column strengthens the décollement beneath the prism, extending co-seismic velocity-weakening behaviour close to the trench, which may occur at other subduction zones with similar sediment compositions, thicknesses and/or temperatures.

Plain Language Summary

In 2004, the plate boundary at the Sumatra subduction zone was ruptured by a very large earthquake. During the earthquake, plate-boundary-fault slip extended unusually far out into the Indian Ocean, causing seafloor uplift in deep water that contributed to the damage caused by the tsunami. Sediments on the incoming plate reach up to 5 km in thickness near the earthquake epicenter. We use data from International Ocean Discovery Program drilling of these sediments and seismic reflection data to show that the deepest sediments are heated to temperatures of >150°C. This drives chemical transformations within minerals that make up the sediments: Minerals lose chemically bound water as they are heated and transformed. This water travels upwards, and is trapped if it meets an impermeable barrier. Observations from seismic data provide an estimate of where and how much water is trapped. Our modelling shows that sufficient water is produced within the last 1 Myr, and that over longer time periods the water has escaped. The interplay between an impermeable barrier and the expulsion of fluids from the sediments affects the level at which the plate boundary forms, and has implications for its behavior during an earthquake.

1 Introduction

Understanding the earthquake potential of subduction zones is critical for assessing their seismic and tsunamigenic hazard and risk. Megathrust earthquakes at subduction zones rupture the plate boundary fault, or décollement, and nucleate within the seismogenic zone that is often regarded as pressure-temperature controlled (e.g. Hyndman et al., 1997). In accretionary subduction zones (where the largest earthquakes tend to be generated), the seismogenic zone has been traditionally thought to occur beneath the forearc basin (e.g. Byrne et al., 1988; Wang and Hu, 2006; Wells, 2003), however recent earthquakes such as Sumatra-Andaman 2004 and Tohoku-oki 2011 indicate much shallower ruptures extending beneath part or all of the accretionary wedge/outer forearc towards the trench (Simons et al., 2011).

The frictional stability of the décollement at a subduction zone depends on dynamic geologic factors such as fluid pressure (e.g. Spinelli and Saffer, 2004; Ranero et al., 2008; Ellis et al., 2015), consolidation state of the surrounding material, and the mineralogy of fault zone materials (Fagereng

and Toy, 2011). Scholz (1998) defined a frictional stability parameter from a rate- and state-variable friction law that depends on material properties and effective normal stress. The friction law is derived from experimental laboratory studies of artificial faults in largely homogeneous materials (e.g. Lockner and Byerlee, 1986; Dieterich, 1972; Rabinowicz, 1958). Seismogenesis is limited to the décollement that exhibits velocity-weakening behaviour (a negative frictional stability parameter ζ) (Scholz, 1998, 2019). The limits (up- and down-dip) to seismic behaviour are the transitions from velocity-weakening (seismic slip) to velocity-strengthening (stable-sliding). Determining real frictional properties for the material of and around the décollement at depth in the dynamic environment of a subduction zone remains extremely difficult since the seismogenic décollement is typically 5-40 km below seafloor.

Various studies have attempted to estimate the width and position of the seismogenic zone at subduction zones, where earthquakes can initiate, often by modelling the thermal regime and comparing the results to observed seismicity/earthquake rupture zones where available, with similar methods used for forecasting where no historic ruptures have occurred (e.g. Hyndman and Wang, 1993 (Cascadia); Hyndman et al., 1995 (Nankai); Hippchen and Hyndman, 2008 and Klingelhoefer et al., 2010 (Sumatra); Smith et al., 2013 (Makran); Gutscher et al., 2016 (Ryukyu)). Seismic imaging techniques are used to define the geometry of the subducting slab and sediment thickness (at the deformation front), and parameters such as convergence rate and plate age, are employed to match the results to seafloor heat flux measurements. Seafloor heat flux values are estimated by shallow heat probe measurements, borehole measurements and/or derived from bottom-simulating-reflectors of gas hydrates. The seismogenic zone is proposed to lie between the 150 and 350 °C isotherms (Hyndman et al., 1997), where 350 °C is the downdip limit at the onset of the brittle-ductile transition (Scholz, 2019).

A key driver to link seismogenesis and thermal state is that thermally-controlled diagenetic and low-grade metamorphic reactions occurring during burial change the frictional properties of sediments (e.g. Vrolijk, 1990). Potential reactions include the smectite to illite transition (e.g. Saffer et al., 2008); the opal to quartz transition (Spinelli and Underwood, 2004); carbonate and zeolite cementation; and hydrocarbon maturation (Moore and Saffer, 2001). These processes consolidate sediments, release fluids and alter sediment frictional properties; they are estimated from laboratory studies to take place over intervals between ~50 and 175 °C (e.g. Ernst, 1990; Mizutani, 1970; Pytte and Reynolds, 1989). In most subduction zones, such temperatures are reached some distance landward of the deformation front, below the forearc. Total completion of these reactions may release volumes of fluid up to 29 % of the original mineral volume for opal and 40 % for smectite (Hüpers et al., 2017).

The temperature of the décollement sediments (or the sediment-basement interface; sometimes the position of the décollement) depends on sediment burial history. Where the sediment column is sufficiently thick on the incoming plate, basal sediments have been proposed to reach the temperatures of these diagenetic and low-grade-metamorphic reactions, before sediments enter the subduction zone (e.g. Spinelli and Underwood, 2004; Ike et al., 2008; Smith et al., 2013; Hüpers et al., 2017). This has led to the hypothesis that thick input sediments can bring the change from velocity-strengthening (stable-sliding) to velocity-weakening (seismic slip) (the updip limit of seismogenesis) further updip, by drawing the onset of mineral transformations and associated cementation seaward and increasing the potential seismogenic width and thus earthquake magnitude (e.g. Moore and Saffer, 2001; Saffer et al., 2008; Dean et al., 2010; Smith et al., 2012). Such a "shallow" rupture also increases the size of a potential tsunami as rupture extends into deeper water above the outer forearc.

1.1 Tectonic Setting

The Sunda subduction zone extends from Bali to the Andaman Islands, and forms by normal to oblique subduction of the Indo-Australian plate beneath the Sunda plate. In the north (offshore North Sumatra and the Nicobar Islands), the incoming plate sedimentary section reaches thicknesses > 5 km at the trench, thicker than most other accretionary margins, due to the presence of the Bengal-Nicobar Fan system. The succession was sampled on the oceanic plate, ~230 km seaward of the North Sumatra subduction zone by International Ocean Discovery Program (IODP) Expedition 362 (McNeill et al., 2017) (Figs. 1 and 2). It is composed of thick Nicobar Fan deposits that range from clay to fine-grained sand, overlying a basal layer of pelagic and tuffaceous sediments. The sediments are mostly poorly consolidated and unlithified, except for the deepest intervals. IODP drilling also encountered intrusive and extrusive igneous intervals within the deepest units overlying oceanic basement at Site U1480; these units are ~10 Myr younger than the 68-Myr-old oceanic basement (Fig. 3; Backman et al., 2019) and are probably associated with volcanic activity on the flanks of the Ninety East Ridge (NER). This has important implications for the thermal evolution of the sedimentary succession, which we explore in this paper.

The 2004 M_w 9.2 Aceh-Andaman earthquake ruptured ~1600 km of the northern segment of the Sunda subduction zone. Coseismic slip during the earthquake reached far seaward beneath the accretionary wedge, and potentially to the trench (Bletery et al., 2016), and the extensive rupture and large coseismic slip resulted in a tsunami that claimed over 250 000 lives (Lay et al., 2005). Towards the southern end of the rupture zone, Dean et al. (2010) identified a high-amplitude, negative polarity (HANP) seismic reflector at depth within the incoming plate sediments, which is interpreted to develop into the plate boundary fault. We hereafter refer to the HANP as polarity reversal on reflector R11 (Fig. 2). Dean et al. (2010), Geersen et al. (2013) and Gulick et al. (2011) have argued that this

seismic character indicates diagenetic fluid generation at depths of 2-3 km, occurring in the thick input sediments before subduction. The along-subduction zone extent of this reflector broadly corresponds to a region of unusual prism structure and morphology, interpreted to also result from unusual material and basal properties (e.g., McNeill and Henstock, 2014). Beneath the accretionary prism, the reflector becomes less reflective, suggesting fluids have been released along prism faults (Dean et al., 2010).

IODP Expedition 362 identified reflector R11 as the downward transition from predominantly fan to pelagic sediments, and found geochemical evidence for recent release of fresh water at depth in the boreholes, interpreted as diagenetic fluid release having already started even >200 km from the subduction zone (Hüpers et al., 2017; McNeill et al., 2017). Hüpers et al. (2017) used thermal hydrogeologic modelling to show that these fluids were likely produced through dehydration of amorphous silica, where this reaction would be complete before the basal sediments reach the trench. They also predict that the smectite to illite clay dehydration reaction would be almost entirely complete before the basal sediments entered the subduction zone. This differs from other accretionary margins, e.g. Nankai and the Lesser Antilles/Barbados, where hydrogeologic models show that smectite dehydration at the level of the décollement begins and ceases below the forearc (Moore and Saffer, 2001; Saffer and Tobin, 2011).

In this study, we build on the work of Hüpers et al. (2017) by investigating the thermal structure and evolution of the entire sediment section on the North Sumatra incoming plate between the NER and the subduction zone deformation front. We combine multichannel seismic (MCS) data with ground-truthed material properties data from IODP sites in the input section of the subduction zone (Fig. 1) and use a time-varying thermal model (Hutnak and Fisher, 2007) to determine temperature on the seismic profiles through time offshore the rupture area of the 2004 earthquake, testing a range of parameters to examine uncertainties. Using this thermal history model we map the progression of diagenetic dehydration reactions through the sediment column during its deposition, and estimate the amount of fluid liberated from the basal sediments that underlie reflector R11. We subsequently test the likelihood of the unusually thick sedimentary section generating a shallow seismogenic updip limit and increased earthquake rupture area.

2 Methods

2.1 Datasets

We use MCS data from the northern Wharton Basin (Fig. 1, Geersen et al., 2013; McNeill et al., 2017) and core and log data from IODP Expedition 362 boreholes (Fig. 1, Dugan et al., 2017; McNeill et al., 2017). The seismic data are from Gaedicke (2007; cruise SO186-2 of the SEACAUSE campaign on FS Sonne, with data jointly owned by German and Indonesian institutions) and porosity,

biostratigraphic and gamma ray data are from IODP Expedition 362 Sites U1480 and U1481. We also incorporate regional seafloor heat flux data, derived from the World Heat Flow Data Collection (Jessop, 2012).

2.2 Sedimentary parameters

Borehole sediment properties were correlated onto and along the seismic profiles, i.e. stratigraphic age and boundaries, lithology, velocity, porosity, natural gamma ray/radiogenic element composition, thermal properties and direct comparison of seismic with core and log properties.

The subparallel, laterally-continuous seismic reflectors can be confidently traced along most of each seismic section (Fig 2). We interpret 14, roughly evenly-spaced reflectors R1-R14, in accordance with the interpretation of Pickering et al. (2020), and correlate these from the drill sites to the subduction zone deformation front and between the two profiles (using a third crossing seismic profile, not presented here). Reflector R11 is the horizon that develops into the HANP pre-décollement reflector of Dean et al. (2010). We interpolate the depth-converted positions of these reflectors at Site U1480 (see below for velocity information) and apply ages from the borehole stratigraphy to provide chronology for the seismic stratigraphy, assuming that the reflectors are isochronous along the profile. Reflector R2 onlaps onto reflector R3 within the trench wedge, and is therefore not intercepted at the IODP drill sites further seaward, we estimate an age for this reflector of ca. 1.0 Ma based on the average sediment accumulation rate through the trench and our depth-conversion of the reflectors. Reflector R13 is not resolvable in the seismic data at Site U1480, so is also excluded because its age cannot be reliably defined.

Three major units A, B and C are interpreted (note these differ from the lithostratigraphic units of IODP Expedition 362). Unit A (Figs. 2 and 3), the wedge filling the subduction trench (the trench wedge), is ~2500 m thick at the deformation front, but only 140 m thick at Site U1480. It is composed of calcareous clays, fine grained sand, silty sand and clay, minor calcareous ooze and ash at the borehole location but these lithologies may differ in the trench, and it is bound by the seafloor (R1) and reflector R4. At the location of U1480 our Unit A corresponds to all of IODP Expedition 362 lithostratigraphic Unit I and uppermost Subunit IIA. Unit B consists of Nicobar Fan thin- to medium-bedded predominantly siliciclastic silts, clays, and fine-grained sands, bound by reflectors R4 and R11, which is ~1100 m thick at Site U1480 (our unit B corresponds to most of IODP 362 Subunit IIA, and all of subunits IIB and IIC) and ~1800 m thick at the deformation front. Unit C is the deepest, between reflector R11 and the top of oceanic basement (R14); at Site U1480 this is an ~150 m thick interval that consists of mostly pelagic claystones, minor chalk and tuffaceous material, includes semi-lithified and lithified materials and has a relative lack of terrigenous siliciclastic sediments (our Unit C corresponds to IODP 362 Units III-V in McNeill et al., 2017). The sediments of Unit C slowly accumulated over a period of ~50 Myr, whereas the overlying 1250 m of Units A and B (at Site

U1480) accumulated rapidly over ~9 Myr (McNeill et al., 2017; Backman et al., 2019). The total sediment thickness changes from ~1400 m at Site U1480 to a maximum of ~5100 m at the deformation front on seismic profile 1 (Fig. 3), primarily due to thickening of Unit A. Shallow sediment accumulation rates therefore increase dramatically within Unit A as the plate approaches the subduction zone.

2.3 Regional heat flow

The oceanic crust on the profiles formed at ~70-60 Ma (Figure 1; Jacob et al., 2014). Inset C in Figure 1 shows predicted surface heat flow based on the Stein and Stein (1992) oceanic plate cooling model, and available seafloor heat flux probe measurements from Jessop (2012) plotted against the age of the oceanic crust at their location (Müller et al., 2008), including from temperature measurements made in the IODP Expedition 362 boreholes (McNeill et al., 2017). There is significant scatter in the data, although there is some clustering around the predicted heat flux values. Plate cooling models (e.g., Stein and Stein, 1992) assume that all heat transfer is conductive, and do not account for heat transfer via convective water circulation. Seafloor probe heat flux measurements are also subject to factors that may bias measurements e.g. the tilt of the instrument as it enters the sediment and near surface effects such as local fluid flow at faults (Stein and Abbott, 1991). This is particularly important where oceanic basement rocks are exposed, or sediment cover is thin, and convection is strong (Stein and Abbott, 1991; Hutnak and Fisher, 2007), e.g. at the NER and may account for anomalously high heat flow values there (Fig. 1). Near Site U1480, the surface heat flux probe measurement from Jessop (2012) is 96.3 mWm^{-2}. In contrast, advanced piston corer temperature tool (APCT-3) formation temperature measurements in Hole U1480E to a depth of ~200 mbsf (metres below seafloor) generate an estimated surface heat flux of 72.6 ± 5.1 and 75.0 ± 6.6 mWm^{-2}, using a Bullard plot, and the temperature gradient and thermal conductivity, respectively with errors given at the 95% confidence interval. There are numerous faults within the sedimentary column in the Expedition 362 borehole area (e.g., Geersen et al., 2015; Stevens et al., 2020) that could generate anomalous heat flow values, but Site U1480 is >500 m away from the nearest seismically resolvable fault. We therefore argue that the heat flux estimates generated from the borehole APCT-3 measurements are more reliable than the seafloor measurements. We test our thermal models at Site U1480 against these different estimates, however in the absence of a series of drilling-controlled heat flux measurements towards the deformation front, we also compare our model results with the seafloor probe measurements from Jessop (2012).

2.4 Thermal modelling and input parameters: Time-Depth Conversion, Thermal Rejuvenation and Radiogenic Heat Production

Thermal models of the sedimentary section were constructed using the SlugSed one-dimensional fluid and heat transport modelling software coded in MATLAB (Hutnak and Fisher, 2007). This model

uses accumulation rates of sediment layers, where the sediment-basement interface subsides and creates accommodation space in which sediment accumulates and compacts by a user-specified porosity-depth function. We define the sedimentary layers between the seafloor (reflector R1) and reflector R14 (excluding reflectors R2 and R13, see above), and use a porosity-depth function derived from the measurements made at Site U1480. We construct one-dimensional models at broadly evenly-spaced localities along each seismic profile (approximately 1000 common depth points (CDPs) apart, where CDP spacing is 6.25 m). At each model locality, we depth-convert interpreted horizons to return sedimentary layer thicknesses in metres. Depth conversion was performed on horizon picks (as opposed to applied to the entire MCS data – we only required horizon depths at discrete locations) using interval velocities derived from the original seismic processing (at approximately 1000 CDP intervals). These velocities are not derived from tomographic studies, however they show gradual lateral changes, are consistent with the core-log-seismic integration following drilling at Sites U1480 and U1481 (McNeill et al., 2017), and are similar to velocities determined nearer the trench (Qin and Sing, 2017). We clip the maximum seismic velocity within the sedimentary section to 4.5 kms^{-1}, consistent with Qin and Singh (2017) and Ghosal et al. (2014). This produces a basement depth at the trench of ~10 km below sea level, consistent with Singh et al. (2012). Nevertheless, uncertainties in seismic velocity could be a source of error in our models, and therefore we test the effect of varying velocities by ± 15% which we consider exceeds the true error bounds (results for ± 15% velocities are presented in the supporting information).

Each one-dimensional model is stressed as the simulated sedimentary layers accumulate between the seafloor and a subsiding sediment-basement-interface where an evolving basal heat flux is applied. We apply a heat flux that decays with a $1/\sqrt{time}$ relationship, based on the Stein and Stein (1992) thermal model for the oceanic lithosphere. In this study, our focus is on the thermal state of the sediments (as opposed to the shallow oceanic crust). So although there are other lithospheric cooling models available (e.g., McKenzie et al., 2005), the good fit between the Stein and Stein (1992) model and global seafloor heat flux measurements suggests it is appropriate for our study.

Extrusive igneous intervals at Site U1480 (Unit IV, Fig. 3C) that are ~10 Myr younger than the 68 Ma oceanic basement (McNeill et al., 2017; Backman et al., 2019) indicate active magmatism at the NER ~58 Ma. We suggest that such magmatism is related to a melting event that occurred after formation of the oceanic lithosphere. We have tested the effect of a thermal rejuvenation of the lithosphere at 58 Ma, i.e., an increase in/reset of the basal heat flux to the level expected at the formation of the oceanic basement that affects the thermal evolution of the sedimentary section. We assume a melting event at the NER influences locations within ~100 km of the NER flank (~275 km from the NER center), based on typical plate thicknesses.

The Expedition 362 results provide ground truth of sediment material properties that we incorporate into the model. We use core porosity data and thermal conductivity measurements from Site U1480 to define bulk thermal conductivity for the sediment column. The thermal conductivity measurements for most of the core samples (particularly mud and calcareous samples) can be fit either to a porosity-controlled geometric mean model (e.g., Lovell, 1985; Fig. S4) using a sediment grain thermal conductivity of 3.0 W $m^{-1}K^{-1}$ and a bulk conductivity defined by the proportion of solid sediment grains to pore fluid, or with no clear depth trend or correlation with porosity. We used the geometric mean for the models presented here, but also tested how surficial heat flux is affected by using an average of the core measurements as a single bulk conductivity throughout the sediment column (see supporting information Text S1.5 and Fig. S5).

The modelled sediments are thermally equilibrated between the sediment-basement interface and the seafloor, which is held at a constant temperature of 1.25 °C from IODP seafloor measurements (McNeill et al., 2017). Basal sediments are heated by the geothermal gradient as the sediment column thickens. We also include radiogenic heat production from the sediments estimated from natural gamma downhole log measurements at Site U1481 (Fig. 4) using an existing method to convert natural gamma ray (NGR) API (American Petroleum Institute) counts (recorded by downhole NGR instruments) to heat production in μWm^{-3} (Bücker and Rybach, 1996). Core sample NGR measurements made at both Sites U1480 and U1481, support that radiogenic properties are similar between the sites. In our calculations of heat production, we exclude samples where the caliper is at maximum reach, i.e., where the borehole wall is washed out or collapsed. This risks excluding the NGR values of lithologies prone to being washed out, e.g., sandy sections, however, Site U1480 NGR core measurements suggest that NGR does not vary significantly with lithology or depth (Fig. S6). Our analysis of the NGR logs for Site U1481 indicates average radiogenic heat production values of 1.37 and 1.54 μWm^{-3} for Units B and C, respectively. Unit A was not logged, but core NGR measurements on IODP lithostratigraphic Units I and II are similar to each other (varying between 20 to 80 counts/s for Unit I and 30 to 90 counts/s for Unit II (McNeill et al., 2017)), suggesting Unit A probably produces a similar radiogenic heat to Unit B.

For thermal capacity of sediment grains and seawater (not available from borehole data), we use data from an analogous environment where these measurements were made on similar lithologies (Goto and Matsubayashi, 2009).

2.5 Dehydration calculations

We run our 1D models to generate temperatures for the entire height of the sediment column at each model locality at 10000-year time steps. For reflectors R1 – R14 (where R1 is present-day seafloor, and R14 is top of basement; R13 is excluded) we extract time-depth and time-temperature history at each model location by tracing depositional history of these horizons through the model domain. We

account for compaction by finding the 'bulk-sediment-velocity' from the harmonic mean of sediment-grain- and pore-water-velocity (see Hutnak and Fisher, 2007). We then assess the progress of diagenetic, thermally-controlled mineral dehydration, by applying reaction kinetics to the temperature histories of each reflector. For the two-step process of amorphous silica dehydration, where opal-A is transformed to opal-CT, and opal-CT to quartz we use the kinetic expressions of Mizutani, (1970), in which the rate of change in the molar fractions of Opal-A (*OA*), and Opal-CT (*OCT*) abundance is given by equations 1a and 1b, respectively:

$$\frac{\partial OA}{\partial t} = -A_{OA} \cdot e^{-\frac{E}{RT}} \cdot OA$$

Equation 1a

$$\frac{\partial OCT}{\partial t} = -A_{CT} \cdot e^{-\frac{E}{RT}} \cdot OCT$$

Equation 1b

Where *OA* and *OCT* are the mole fractions of Opal-A and Opal-CT from the previous time step (1 and 0, respectively at the time of deposition), *A* is the frequency factor (A_{OA} = 7.51×10^{-4} s^{-1} and A_{OCT} = 2.30×10^{-4} s^{-1}), *E* is the activation energy (*E* = 6.69×10^{4} J mol^{-1}), R is the gas constant (J mol^{-1} K^{-1}) and *T* is temperature (K). We then calculate the rate at which fluid volume is generated (V_{silica} (unit volume s^{-1})) by these reactions using equation 2 (Kimura et al., 2012):

$$V_{\text{silica}} = \left(\frac{\partial OA}{\partial t} \cdot (H_{OA} - H_{OCT}) + \frac{\partial OCT}{\partial t} \cdot \left(H_{OCT} - H_{QTZ}\right) \right) \cdot OA_i \cdot h \cdot (1 - n) \cdot \frac{\rho_{sed}}{\rho_{iw}}$$

Equation 2

Where *H* is water content of the three silica phases (2.1-12.1 wt% for Opal-A, average 7.3 wt%; 1.0-8.9 wt% for Opal-CT, average 5.5 wt% (Day and Jones, 2008) and 0.4 wt% for Quartz (*QTZ*) (Graetsch, 1994)), OA_i is the initial content of opal-A in the bulk sediment (we use a value of 18 wt%, which Hüpers et al. (2017) showed is required to explain pore water freshening at Site U1480), *n* is porosity, *h* is the thickness of the dehydrating sediment column; ρ_{sed} is the density of sediment grains, and ρ_{iw} is the density of interlayer water (we assume 2700 and 1030 kg m^{-3}, respectively). For the smectite to illite transformation, separately we apply both the reaction kinetic derived by Huang et al. (1993) from laboratory experiments at high temperatures, and a range of potassium ion concentrations (*T* = 250-325°C, [K^+] = 100-3000 mM) (equation 3a); and the reaction kinetic derived by Pytte and Reynolds (1989), which incorporates a synthesis of field data, and fitted to observations of the reaction progress from a wide range of thermal histories in different geological settings, with peak temperatures from 70-250°C and sediment ages ranging from *ca.* 10 yr to 300 Myr (equation 3b):

$$\frac{\partial S}{\partial t}_{\text{Huang}} = -A_{S-\text{Huang}} \cdot e^{-\frac{E}{RT}} \cdot S^2 \cdot [K^+]$$

Equation 3a

$$\frac{\partial S}{\partial t}_{\text{Pytte}} = -A_{S-\text{Pytte}} \cdot e^{-\frac{E}{RT}} \cdot S^5 \cdot \left(\frac{[K^+]}{[Na^+]}\right)$$

Equation 3b

Where S is the molar fraction of smectite in the Illite-Smectite (I/S) mixed layer from the previous time step (we assume S = 0.8 at the time of deposition), and A_S is the frequency factor ($A_{S\text{-Huang}}$ = 8.08×10^4 s^{-1}, $A_{S\text{-Pytte}}$ = 5.2×10^7 s^{-1}). In our application of equation 3a we use a value of 2 mM for $[K^+]$, as indicated by the shipboard geochemical measurements of pore waters at Site U1480 (McNeill et al., 2017). In equation 3b, $[K^+]/[Na^+]$ varies with temperature in the relationship:

$$\frac{[K^+]}{[Na^+]} = 74.2 \cdot e^{\frac{-2490}{T}}$$

Equation 3c

This assumes that the ratio $[K^+]/[Na^+]$ is in equilibrium with K-feldspar (Pytte and Reynolds, 1989). To assess the volume of water expelled by the smectite to illite transformation, we apply equation 4 (Saffer and McKiernan, 2009):

$$V_{\text{smectite}} = \frac{\partial S}{\partial t} \cdot \frac{H_S}{1 - H_S} \cdot S_i \cdot h \cdot (1 - n) \cdot \frac{\rho_{sed}}{\rho_{iw}}$$

Equation 4

Here H_S is the water content of smectite (we assume H_S = 20 wt%, where the smectite water interlayer basal d-spacing is 15 Å (Bird, 1984)), and S_i is the initial mass fraction of smectite in the bulk sediment. We separately tested rate parameters from equations 3a and 3b to assess the impact of using the Huang et al. (1993) and Pytte and Reynolds (1989) reaction kinetics, respectively. The IODP Expedition 362 results indicate the bulk sediment is composed of 65 wt% clays (McNeill et al., 2017), where we assume 80% is smectite (from S = 0.8 in I/S mixed layer). This is consistent with the measurements of Rosenberger et al. (2020) at Site U1480. However, we acknowledge that their measurements at Site U1481 showed a lower proportion of smectite, which would reduce the fluid expulsion rates by a factor of 2. It has been suggested that oven drying of samples may produce artificially high porosity results (Brown et al., 2001); Brown and Ransom (1996) defined a porosity correction which we choose not to use. The Brown and Ransom (1996) correction would increase the grain-to-pore-space ratio, i.e. increase the value of (1 - n) in equation 4, so in that respect our calculations likely underestimate the released fluid volume.

In addition to assessing the progression of dehydration reactions at individual reflectors (e.g., at R11/the décollement level), by running the depositional history of each reflector through these equations, we reconstruct the dehydration state (in terms of rate of fluid expulsion per unit volume for silica/smectite) of the entire incoming sediment section at specific time steps e.g., prior to deposition of the Nicobar Fan, immediately before development of the trench wedge, and at the present day (see section 3.3).

3 Results

3.1 Initial thermal model tests

The primary variables in our model are: sediment accumulation rate; radiogenic heat production; and timing of the imposed basal heat flux. Sediment accumulation rates are controlled by our seismic interpretation and the age model (Fig. 3). The effect of variation in sediment accumulation rates is tested through the application of ± 15 % picked velocities within the sediment column in time-depth conversion (see section 2.4). To test the effects of radiogenic heat production within the sediment column and rejuvenation of the basal heat flux, we ran repeat one-dimensional models at the location of Site U1480. We compare our temperature and surface heat flux results from repeat model runs with IODP measurements, to assess their validity and derive a best estimate. The IODP measurements indicate that the geothermal gradient within the shallowest ~200 m of sediments at Site U1480 is ~44.4 °C km^{-1} with a surface heat flux of 72.6 ± 5.1 $mW.m^{-2}$ (lower estimate) (McNeill et al., 2017). Extrapolation of this thermal gradient down to basement depths suggests a temperature at the sediment-basement interface at Site U1480 of ~60 °C.

An initial model stressed over 11 periods of sediment accumulation defined by the seismic reflectors, applying no radiogenic heat production within the sediment column and using a basal heat flux decaying from the basement age of 68 Ma predicts a present-day seafloor heat flux of 62 mWm^{-2}. This is consistent with the predictions of the Stein and Stein (1992) model, but is lower than the borehole-derived estimation, indicating additional processes are required to generate higher heat flux. We therefore tested the effects of radiogenic heat production and lithospheric thermal rejuvenation on surface heat flux.

We applied a sediment radiogenic heat production value of 1.3 $\mu W.m^{-3}$ throughout the sediment column, based on NGR log data (average derived value, see above, Fig. 4). This results in a present day seafloor heat flux of 63 mWm^{-2}. Due to the remaining significant discrepancy with the lower borehole-derived estimate of 72.6±5.1 $mW.m^{-2}$, we assessed what level of radiogenic heat production within the sediment column would be required to match our model output to the borehole-derived estimate. Only when ~9 $\mu W.m^{-3}$ radiogenic heat production is applied throughout the sediment column do we attain a surface heat flux value of 72.6 $mW.m^{-2}$ (all other parameters unchanged). This

far exceeds heat production values typical of any sediment type (e.g. siltstones 1.8 μWm^{-3}) (Rybach, 1986) including those encountered at Site U1480, and equates to a NGR API reading of 570 (Bücker and Rybach, 1996) whereas measured values at Site U1481 are < 150 API (Fig. 4). We conclude that radiogenic heat production within the sediment column makes only a minor contribution to the resulting thermal structure and seafloor heat flux.

We assume that 1.3 $\mu W.m^{-3}$ is a good approximation of radiogenic heat produced within the sediment column, and subsequently tested the effect of a perturbation to the imposed basal heat flux. During the course of the model (which starts at a basement age of 68 Ma) we reset the basal heat flux to the initial value (510 $mW.m^{-2}$, Stein and Stein, 1992) at 58 Ma – representing the effect of lithospheric rejuvenation coeval with volcanic lava flows in Unit IV at Site U1480 (Backman et al., 2019). This 'thermal rejuvenation' generates a final surface heat flux of 68 mW m^{-2} at the location of Site U1480, which is now within the 95% confidence level of the lower borehole-derived heat flux estimate (72.6 ± 5.1 $mW.m^{-2}$). The combination of thermal rejuvenation and sediment radiogenic heat production results in a basement temperature of 56.6°C (average thermal gradient ~42°C km^{-1}). These results are generally consistent with Hüpers et al. (2017) (~60°C at the base of IODP lithostratigraphic Unit III and a geothermal gradient of 44.4°C.km^{-1}). Therefore, we suggest lithospheric thermal rejuvenation played a key role in the thermal history of the sediments currently at and near to the location of Site U1480, in a similar mechanism to that recognised for Hawaii by Detrick and Crough, (1978).

3.2 Burial history

Following the model tests described above, we apply a best estimate of parameters to the entire incoming sediment section and model its time evolution as it approaches the subduction zone. Sediment accumulation rates increase towards the deformation front controlled by the increasing thickness of seismic packages between reflectors. Radiogenic heat production through the sediment column is based on the measured NGR log values. A lithospheric thermal rejuvenation event is applied to all model localities within 100 km of the NER.

We highlight the results from 3 localities on seismic profile 1: at 68 km (Site U1480), 195 km (Pseudo site 1) and 290 km (Pseudo site 2) along-profile (232, 100 and 5 km from the deformation front, respectively) (Fig. 5, locations on Fig. 2). In Figure 5 we present the burial and temperature history, and dehydration reaction progression at the R11 or pre-décollement level since the deposition of R11 at 9.3 Ma. Pseudo site 1 is the position at which R11's reflection polarity becomes reversed; and Pseudo site 2 is our closest model to the deformation front. Lateral variation in the sediment thickness between seismic reflectors results in different sediment accumulation rates for some time periods (i.e., the gradients of the burial depth curves in Fig. 5A-C) between the three pseudo site localities. Seismic velocities within the deepest sediments close to the deformation front are the least certain, so potential errors in the time-depth conversion are highest here.

3.3 Temperature structure and progression of mineral dehydration through the sediment column

From the sediment column temperatures generated by our models at each model locality, we reconstruct a two-dimensional (2D) grid of temperatures for the entire incoming sedimentary section at specific time steps (Fig. 6), specifically: 9.3 Ma (R11), onset of Nicobar Fan deposition; 2.2 Ma (R4), onset of main trench wedge deposition; 1.0 Ma (R2), the approximate time of maximum fluid generation beneath R11 at Pseudo site 2 due to clay mineral dehydration (based on the Pytte and Reynolds (1989) kinetic); and the present day (R1). Accumulation of the >2 km thick trench wedge is largely responsible for the high basal temperatures close to the deformation front, reaching >100°C. However, from Pseudo site 1 to the deformation front, temperatures of ~100°C are already reached within basal sediments that underlie R11, before the start of trench wedge deposition (Fig. 6C). For each time step we also extract the surface heat flux across seismic profile 1 (Fig. 6A). As expected, surface heat flux is much higher where we apply a thermal rejuvenation. The surface heat flux is generally consistent with predictions of the Stein and Stein (1992) model, with some variation related to basement topography. However, during the development of the trench wedge, where trench wedge sediments are thickest (~250 km along-profile towards the deformation front), there is a significant decrease in the surface heat flow and deviation from the global values due to the blanketing effect of the young sediments (also see Fig. S5).

Figure 5 D-E shows the molar fraction change for the modelled dehydration reactions for Site U1480 and for Pseudo sites 1 and 2. The associated rate of fluid expulsion due to these mineral reactions is presented in Figure 5 G-I. At Site U1480 our results suggest that the opal to quartz reaction is still ongoing, with a maximum fluid production rate due to silica dehydration of $\sim 0.2 \times 10^{-15}$ s^{-1} (per unit volume of bulk sediment) ca. 1.7 Ma, consistent with Hüpers et al. (2017), since when this process becomes the largest fluid source. Our calculations also imply that the smectite-illite reaction has yet to begin at Site U1480, consistent with Hüpers et al. (2017). At Pseudo site 1, the modeled opal-quartz reaction is complete by the present-day. Compaction remains the largest source of fluid release throughout burial history at this location, however, the smectite-illite reaction starts around the onset of trench-sediment deposition (2.2 Ma). Higher sediment accumulation rates earlier in the burial history of Pseudo site 2 (and associated early more rapid increase in temperature) leads to earlier onset and completion (prior to trench wedge development) of the opal-quartz reaction (Fig. 5F). The smectite-illite reaction begins just before the onset of trench wedge development, and accelerates rapidly at 2.2 Ma, becoming by far the dominant fluid source over the most recent time periods. The Pytte and Reynolds (1989) kinetic suggests that fluid expulsion from the smectite to illite transformation peaks ca. 1.0 Ma (the approximate age of reflector R2), whereas the Huang et al. (1993) kinetic suggests it peaks within the last 200 kyr (Fig. 5I).

Our reconstructions of the dehydration state of the incoming sediment section are presented in Figures 7 (for smectite dehydration, Pytte and Reynolds (1989) kinetic (see Fig. S8 for results using the Huang et al. (1993) kinetic)) and S7 (for silica dehydration). Some fluid is produced through amorphous silica dehydration within the basal sediments in the present day around the location of Site U1480 (Hüpers et al., 2017). However, towards the deformation front, and particularly near where R11 becomes reversed polarity, silica dehydration predominantly occurs shallower than R11, ~1-2 km below the seafloor (even when ±15% velocities are used in the seismic time-depth conversion). Our results suggest diachronous completion of the silica dehydration reaction within the basal sediments that underlie R11, where burial activated the reaction progressively further seaward, with the reaction complete in the furthest seaward of these sediments (~250 km) shortly after 2.2 Ma.

In contrast, our reconstructions for smectite dehydration suggest that this reaction was only just beginning within basal sediments at 2.2 Ma. We calculate that, approximately halfway through the deposition of the current trench wedge sediments at 1.0 Ma, fluid expulsion from smectite dehydration was focussed at the R11 (or pre-décollement) level, (dashed line in Figs. 7C-E (at zero depth in B)), in the region where we observe reversed polarity on the reflector in the present day. Our reconstruction for the present day indicates that, by this time, beneath the trench wedge, smectite dehydration has progressed to the sediments immediately above R11 (Fig. 7E). This implies that the basal sediments currently at the deformation front are fully dehydrated, before entering the subduction zone. Figure 7A shows the corresponding thickness of fluid produced by the basal sediments (underlying R11, dashed line) along seismic profile 1 (a cumulative plot of the total fluid from the reaction, showing the contribution from each time period is shown in Fig. 8D). We calculate that, where R11 polarity is reversed, similar thicknesses of fluid are generated in the period from 1.0 Ma to the present compared to the much longer 9.3-2.2 Ma period, and that ca. 50% more fluid is generated in the 1.0 Ma to present day period than the 2.2-1.0 Ma period. These results suggest a very strong correlation between where fluid is being generated by smectite dehydration in the last 1 Myr and the region of reversed polarity on reflector R11 (the pre-décollement reflector). This correlation is even more pronounced when we apply the Huang et al. (1993) reaction kinetic (Fig. 8C) and remains robust when ±15 % velocities are used in the seismic time-depth conversion (Figs. S8-S12).

4 Discussion

4.1 Heat flux across the incoming section

We compared our model results to regional measurements of seafloor heat flux, by extracting heat flux across the shallowest 2 m of sediment from each 1D model used to build the 2D thermal structure of the incoming sediment section (Fig. 6A). The thermal rejuvenation event applied within 100 km of the flank of the NER increases heat flux values above those expected for the plate age (Stein and Stein, 1992). From ~125 – 250 km along-profile, our results (60 – 63 mWm^{-2}) match the expected

values (61.8 mWm^{-2}) and the closest probe measurement (61 mWm^{-1}, Jessop (2012), Fig. 1B). However, within 40 km of the deformation front, seafloor heat flux from our models decreases slightly within the last 2.2 Ma. The high sediment accumulation rates (SAR), especially within the trench (≥1000 m Myr^{-1}, Fig. 3, S5I), suppress the surficial heat flux relative to the basal input (Fig. S5). At Site U1480, maximum SARs ~225 m Myr^{-1} between 2.6 and 1.7 Ma suppress the seafloor heat flux by only around 1.3%, and after the SAR slows to <20 m Myr^{-1} at 1.7 Ma, the heat flux rebounds. At Pseudo Site 1, higher SARs since 2.2 Ma (up to 400 m Myr^{-1}) result in ~2.5% suppression, by the present day. At Pseudo Site 2, where SARs are much greater since 2.2 Ma (~1000-1700 m Myr^{-1}), the present-day model seafloor heat flux is suppressed by ~15% (Fig. S5C) (or 17.5% using a constant bulk sediment conductivity).

Hutnak and Fisher (2007) modelled that sediment accumulation rates of 500 m Myr^{-1} may suppress the surface heat flux by as much as 32%, and Hutchison (1985) suggests that a SAR of 1000 m Myr^{-1} would suppress the heat flux by as much as 55%. However, these studies used a constant SAR over 10 to 20 Myr. Harris et al. (2020) suggested that, at the Cascadia margin, a SAR of ~1300 m Myr^{-1} over ~3 Myr suppresses surface heat flux by >50%, but 10 Myrs is still significantly longer than any period of such high sediment accumulation in our study. For example, at Pseudo Site 2, our highest SAR (1740 m Myr^{-1}) persists for only 0.5 Myr between 2.2 and 1.7 Ma, after which the SAR slows significantly allowing seafloor heat flux to rebound, but not return to equilibrium with the basal input, and then the heat flux continues to decrease. The variable SAR throughout the deposition of the Nicobar Fan and accumulation of the trench wedge, produces multiple instances of seafloor heat flux suppression and rebound (Fig. S5). Should the high SARs within the trench continue into the future (e.g., on the timescales used by Hutchison (1985) and Hutnak and Fisher (2007)), we would expect much greater suppression of the seafloor heat flux. Heat probe measurements at/near the deformation front elsewhere on the Sumatran margin indicate even lower values (Fig. 1; Jessop, 2012) than implied by our models. We suggest that such low values are from measurements taken in areas where: the SAR has been high and more consistent over a longer period; there is anomalously low basal heat flux; or there has been recent slope failure. Slope failure is common close to the steep outer forearc of the Sumatra margin (Tappin et al., 2007), and may have deposited sediment thicker than the probe penetration depth (e.g. 5-10 m), effectively blanketing the seafloor at the point of measurement, the instantaneous SAR would be extremely high compared to the longer term average, disproportionally suppressing heat flux to the seafloor. We also note that radiogenic heat production within the sediment column offsets the suppressing effect of sedimentation e.g., by ~6% at the deformation front (within the last 2 Myr), consistent with Hutchison (1985).

4.2 Mechanisms for trapping of diagenetic fluids and explanation of seismic properties

Full waveform inversion analysis of seismic data within our area (Qin and Singh, 2017) indicates high *P* wave velocities (>4 km s^{-1}) through sediment Unit C (underlying reflector R11) close to the deformation front. To reconcile these high background velocities with the polarity reversal and high amplitude of reflector R11 in seismic reflection data, these authors suggest that the reflector represents a thin (70-80 m) layer anomalously high porosity (~30%, >20% higher than the background level) containing overpressured fluid. This agrees with the ~80 m thick freshening anomaly and increased porosity interval detected at R11 depth at Site U1480 by Hüpers et al. (2017). We suggest that a mobilised fluid source of 'thickness' 20-25 m (30% of 70-80 m) could be trapped at the R11 level and explain the polarity reversal.

Based on our results (Fig. 8), we estimate that, since 9.3 Ma, fluid well in excess of 20-25 m thickness has been generated by compaction and dehydration of the sediments below R11 along most of the length of seismic profile 1 (Fig. 8E), where compaction and the dehydration of smectite as it transforms to illite are the key fluid sources. Our calculations may even underestimate expelled fluid volumes from mineral dehydration, since we do not consider the expansion of mineral-bound water upon its release where its density decreases by ~5% (e.g. Bethke, 1986). However, reflection amplitude and polarity of R11 are only anomalously high and reversed within ~100 km of the deformation front (landward of Pseudo Site 1). If our calculations are accurate and any of the fluid generated seaward of Pseudo Site 1 was focussed into a layer at R11, much of it must have since been drained. Alternatively, Pseudo Site 1 marks the seaward limit of a process that causes trapping of fluid at R11. We propose that this process is cementation within the turbidite-rich sediments of the Nicobar Fan (Unit B) immediately overlying reflector R11. Silica and calcite ions are released as a by-product of the smectite-illite transformation and transferred from shales to sandstones by migration of pore waters, where they then produce quartz overgrowths and calcite cements at temperatures >60°C (Boles and Franks, 1979). This process has frequently been invoked in the context of frictional properties at subduction zone décollements (e.g. Marone and Scholz, 1988; Ikari et al., 2007; Moore et al., 2007; Saffer et al., 2012). Our model of the smectite-illite transformation suggests that in the present day it is ongoing within the sediments immediately overlying R11, where the reflector's polarity is reversed (Fig. 7E), and essentially complete in the underlying sediments. We suggest that fluid expelled from the pelagic claystone sediments of Unit C by compaction and the smectite-illite transformation since ca. 1.0 Ma are focussed (possibly facilitated by pervasive faulting throughout the incoming sediment section (related to the Indian Ocean diffuse plate boundary e.g. Geersen et al., 2013; Stevens et al., 2020) where the faults are un-cemented) into a thin high-porosity layer at the R11 level. Above this level, concomitant cementation turbidite sands within the trench wedge and fan stratigraphy (and locally of cross-cutting fault planes) could create an impermeable seal preventing further upward migration. We also suggest that this supports the argument made by Geersen et al. (2013) that fault planes at R11 depth act as impermeable barriers.

We suggest that in shallower parts of the sediment column above the present-day zone of smectite dehydration (<2000 mbsf, Fig. 7E) there is efficient draining of fluid to the seafloor: we observe no seismic evidence of fluid trapping in this interval, yet we predict recent fluid generation through silica dehydration (Fig. S7). Draining of fluid from the sediment column above R11 is likely facilitated by a combination of relatively porous and permeable (uncemented) fan and trench wedge sediments and pervasive faulting ((e.g., Geersen et al., 2015; Stevens et al., 2020).

4.3 Thermal structure influence on décollement development and seismic behavior

The position of the décollement in the outer forearc ranges in different locations from relatively shallow within the sediment section (e.g. the Mediterranean Ridge/Hellenic subduction zone, Westbrook and Reston, 2002), to the sediment-basement interface (e.g. central Sumatra, Cook et al., 2014). Some margins also exhibit significant along-strike variation in the depth of the décollement e.g. along the Cascadia margin (e.g. Han et al., 2017), and south-central Chile margin (Olsen et al., 2020). The position of décollement formation is thought to be dictated by preferential propagation through frictionally weak intervals in the incoming sediment column, and this control may be lithological, physical, hydrological or a combination (Underwood, 2007).

The North Sumatran example studied here shows apparent combined lithological, diagenetic and hydrological properties controlling the position of décollement formation. Other examples worldwide include the frontal décollement at the Barbados accretionary prism which, from ocean drilling, forms along a frictionally weak radiolarian ooze layer, marking the lithological boundary between pelagic clays below and turbidites above (Moore, 1982; Housen et al., 1996). We note this stratigraphic position is equivalent to that in North Sumatra (boundary between pelagic and turbidite-rich fan sediments). The frontal Cascadia décollement offshore Washington forms in the deep sediment boundary between carbonate clays below and sandy turbidites above interpreted as a weak frictional layer and proposed to drive the observed landward vergence here (Gutscher et al., 2001; Adam et al., 2004). In general in Cascadia, the position and properties of the décollement have been linked to forearc structure (MacKay et al., 1992; MacKay, 1995; Han et al., 2017).

For North Sumatra, we suggest that the depth of the décollement at the deformation front is specifically controlled by the enhancement of a pre-existing lithological boundary deep (~4000 mbsf close to the deformation front) within the incoming sediments. We propose that rapid accumulation of ~2 km of sediment within the trench produces high temperatures in the basal sediments generating and expelling mineral-bound fluid through the smectite-illite transformation and leading to quartz overgrowth and calcite cementation in overlying sands. Liberated fluids get focused within a thin high porosity layer close to the boundary between the pelagic sediments (Unit C) below and Nicobar Fan sediments (Unit B) above, where cemented sand intervals act as an impermeable cap. This could

generate high pore fluid pressure within the layer (e.g. Spinelli and Underwood, 2004), which would reduce the effective stress and enhance frictional weakness (Scholz, 1998), which could then be exploited by the initiating décollement. This subsequently promotes low basal shear stress along a stratigraphically deep frontal décollement, hypothesized to lead to formation of landward-vergent structures in the outermost prism (Dean et al., 2010; McNeill and Henstock, 2014)

Globally, décollement seismic reflectivity and polarity are interpreted as showing presence/absence of change in physical properties across the décollement, either in terms of relative consolidation or pore pressure. For example, in Costa Rica and Nankai-Muroto, the décollement beneath the outer prism is marked by high amplitude, reversed polarity reflections, interpreted as high pore fluid pressures generated by diagenetic dehydration (Bangs et al., 2004; Ranero et al., 2008) representing the outer aseismic section of the plate boundary fault. The seismic properties are similar to those found in the input section offshore North Sumatra outboard of the subduction zone. In the case of North Sumatra, we show that the deepest 1-1.5 km of the sediment column has probably completed the smectite-illite transformation (Figs. 5, 7) and most diagenetic fluids have been generated and escaped prior to subduction. Therefore, once these sediments are accreted or subducted they do not provide a source of diagenetic fluid to resupply the décollement and are largely already quartz-cemented. In the North Sumatra outer prism, the décollement quickly loses its reflection amplitude and reverse polarity landward of the deformation front suggesting fluid rapidly escapes, for example along active prism thrust faults (Dean et al., 2010). This would remove or reduce fluid overpressure at the décollement, increasing plate coupling and promoting strain accumulation; and pervasive quartz-cementation in sands close to the décollement level would act to promote velocity-weakening behavior (e.g. Ikari et al., 2007). We interpret the décollement to have seismogenic potential at this point (Spinelli and Saffer, 2004; Ranero et al., 2008; Saffer et al., 2008; Ellis et al., 2015), within the outer part of the subduction zone (as also proposed by Dean et al., 2010; Gulick et al., 2011; Hüpers et al., 2017). The accretion of a thick, mostly dehydrated sediment column thus generates a strong and cohesive prism and décollement fault capable of transmitting elastic stress far seaward during an earthquake, widening the seismogenic zone and increasing the potential earthquake and tsunami magnitude (e.g. Spinelli and Saffer, 2004).

Our findings support the hypothesis that the thickness of the incoming sediment column has significant implications for its thermal structure and the fluid budget both landward and seaward of the subduction zone deformation front, and the frictional behavior of the décollement (e.g., Spinelli and Underwood, 2004; Saffer et al., 2008). Other subduction zone margins with thick sediment inputs and/or increased temperatures/heat flow such as the Makran (Smith et al., 2013), and parts of the Cascadia (Hyndman et al., 1993; Salmi et al., 2017), Hikurangi (Ghisetti et al., 2016), Lesser Antilles and Hellenic margins (Underwood, 2007), may experience similar pre-subduction sediment dehydration and resulting décollement properties and seismogenic behaviour.

5 Conclusions

Ground-truthed sediment properties from IODP drilling, combined with multichannel seismic reflection data and seafloor heat flux measurements of the incoming sediments offshore North Sumatra, have allowed us to build a detailed model of the thermal structure and dehydration state of the incoming sediments. Our results indicate:

(1) High temperatures within the deeply buried (~5.5 km) basal sediments reach 125-160°C at the ~4.5 km depth of the décollement at the deformation front. This is predominantly due to gradual (but high rate) accumulation of the Nicobar Fan and trench wedge sediments;

(2) Anomalously high heat flux at Site U1480, ~230 km west of the subduction zone can be explained by thermal rejuvenation of the lithosphere ~10 Myr after its formation by magmatism associated with the Ninety East Ridge;

(3) Anomalously low surficial heat flux within the trench is due to the suppressive effect of high rates of sediment accumulation;

(4) Sediment radiogenic heat production has a largely negligible effect on the thermal state of the sediments, but may offset the effects of sedimentation on heat flux through the sediment column by up to 6% for the thickest sediments;

(5) Dehydration over the last ~1 Myr of the basal sediments beneath the horizon that develops into the décollement generates a sufficient volume of fluid to explain the observed reflection polarity reversal of this horizon close to the deformation front, if these fluids are focussed and trapped into a 70-80 m thick high porosity layer;

(6) Silica cementation coincident with the smectite-illite transformation occurs through the deepest (>2000 mbsf) sediments prior to their accretion/subduction. This acts to enhance prism cohesive strength and promote velocity-weakening behaviour at the décollement in the outer prism;

(7) Offshore North Sumatra, combined lithological, diagenetic and hydrological properties appear to control the position of décollement formation deep in the sediment section and at a prominent stratigraphic boundary. Significant pre-subduction dehydration of the incoming sediments excludes these sediments as potential sources of diagenetic fluid within the prism. This impacts the fluid budget of the subduction zone as a whole, and results in the décollement beneath the prism being well-drained and positioned within frictionally strong materials, which may extend the seismogenic zone close to the trench.

6 Acknowledgements

This research used data provided by the International Ocean Discovery Program (IODP). The data on which this article is based are available at http://www.iodp.org/resources/access-data-and-samples, in McNeill et al. (2017). Funding for this research was provided by the Natural Environmental Research Council [grant numbers NE/P012817/1 and NE/L002531/1]. We thank the JOIDES Resolution crew, IODP technical team and science party for their contributions during Expedition 362. In addition, we thank the two anonymous reviewers, associate editor and the editor Whitney Behr for their useful comments, which helped to improve this manuscript.

7 References

Adam, J., Klaeschen, D., Kukowski, N., and Flueh, E., 2004, Upward delamination of Cascadia Basin sediment infill with landward frontal accretion thrusting caused by rapid glacial age material flux: Tectonics, v. 23, doi:10.1029/2002TC001475.

Backman, J., Chen, W., Kachovich, S., Mitchison, F.L., Petronotis, K.E., Yang, T., and Zhao, X., 2019, Data report: revised age models for IODP Sites U1480 and U1481, Expedition 362:, doi:10.14379/iodp.proc.362.202.2019.

Bangs, N.L., Shipley, T.H., Gulick, S.P.S., Moore, G.F., Kuromoto, S., and Nakamura, Y., 2004, Evolution of the Nankai Trough de ´ collement from the trench into the seismogenic zone : Inferences from three-dimensional seismic reflection imaging: Geology, v. 32, p. 273–276, doi:10.1130/G20211.1.

Bethke, C.M., 1986, Inverse hydrologic analysis of the distribution and origin of Gulf Coast-type geopressured zones: Journal of Geophysical Research, v. 91, p. 6535, doi:10.1029/jb091ib06p06535.

Bird, P., 1984, Hydration-phase diagrams and friction of montmorillonite under laboratory and geologic conditions, with implications for shale compaction, slope stability, and strength of fault gouge: Tectonophysics, v. 107, p. 235–260, doi:10.1016/0040-1951(84)90253-1.

Bletery, Q., Sladen, A., Jiang, J., and Simons, M., 2016, A Bayesian source model for the 2004 great Sumatra-Andaman earthquake: Journal of Geophysical Research: Solid Earth, v. 121, p. 5116–5135, doi:10.1002/2016JB012911.

Boles, J.R., and Franks, S.G., 1979, Clay Diagenesis in Wilcox Sandstones of Southwest Texas: Implications of Smectite Diagenesis on Sandstone Cementation: SEPM Journal of Sedimentary Research, v. Vol. 49, doi:10.1306/212f76bc-2b24-11d7-8648000102c1865d.

Brown, K.M., and Ransom, B., 1996, Porosity corrections for smectite-rich sediments: Impact on studies of compaction, fluid generation, and tectonic history: Geology, v. 24, p. 843–846, doi:10.1130/0091-7613(1996)024<0843:PCFSRS>2.3.CO;2.

Brown, K.M., Saffer, D.M., and Bekins, B.A., 2001, Smectite diagenesis, pore-water freshening, and fluid flow at the toe of the Nankai wedge: Earth and Planetary Science Letters, v. 194, p. 97–109, doi:10.1016/S0012-821X(01)00546-5.

Bücker, C., and Rybach, L., 1996, A simple method to determine heat production from gamma-ray logs: Marine and Petroleum Geology, v. 13, p. 373–375, doi:10.1016/0264-8172(95)00089-5.

Byrne, D.E., Davis, D.M., and Sykes, L.R., 1988, Loci and maximum size of thrust earthquakes and the mechanics of the shallow region of subduction zones: Tectonics, v. 7, p. 833–857.

Cook, B.J., Henstock, T.J., McNeill, L.C., and Bull, J.M., 2014, Controls on spatial and temporal evolution of prism faulting and relationships to plate boundary slip offshore north-central Sumatra: Journal of Geophysical Research: Solid Earth, v. 119, p. 5594–5612, doi:10.1002/2013JB010834.

Day, R., and Jones, B., 2008, Variations in water content in opal-A and opal-CT from geyser discharge aprons: Journal of Sedimentary Research, v. 78, p. 301–315, doi:10.2110/jsr.2008.030.

Dean, S.M., McNeill, L.C., Henstock, T.J., Bull, J.M., Gulick, S.P.S., Austin, J.A., Bangs, N.L.B., Djajadihardja, Y.S., and Permana, H., 2010, Contrasting décollement and prism properties over the Sumatra 2004–2005 earthquake rupture boundary: Science, v. 329, p. 207–210.

Detrick, R.S., and Crough, S.T., 1978, Island subsidence, hot spots, and lithospheric thinning: Journal of Geophysical Research, v. 83, p. 1236, doi:10.1029/jb083ib03p01236.

Dieterich, J.H., 1972, Time-dependent friction in rocks: Journal of Geophysical Research, v. 77, p. 3690–3697, doi:10.1029/JB077i020p03690.

Dugan, B., McNeill, L., and Petronotis, K., 2017, Sumatra Seismogenic Zone-The role of input materials in shallow seismogenic slip and forearc plateau development:

Ellis, S., Fagereng, Å., Barker, D., Henrys, S., Saffer, D., Wallace, L., Williams, C., and Harris, R., 2015, Fluid budgets along the northern Hikurangi subduction margin, New Zealand: The effect of a subducting seamount on fluid pressure: Geophysical Journal International, v. 202, p. 277–297, doi:10.1093/gji/ggv127.

Ernst, W.G., 1990, Thermobarometric and fluid expulsion history of subduction zones: Journal of Geophysical Research, v. 95, p. 9047–9053, doi:10.1029/JB095iB06p09047.

Fagereng, Å., and Toy, V.G., 2011, Geology of the earthquake source: an introduction: Geological Society, London, Special Publications, v. 359, p. 1–16, doi:10.1144/SP359.1.

Geersen, J., Bull, J.M., McNeill, L.C., Henstock, T.J., Gaedicke, C., Chamot-Rooke, N., and

734 Delescluse, M., 2015, Pervasive deformation of an oceanic plate and relationship to large >
735 Mw8 intraplate earthquakes: The northern Wharton Basin, Indian Ocean: Geology, v. 43, p.
736 359–362, doi:10.1130/G36446.1.

737 Geersen, J., McNeill, L., Henstock, T.J., and Gaedicke, C., 2013, The 2004 Aceh-Andaman
738 Earthquake: Early clay dehydration controls shallow seismic rupture: Geochemistry,
739 Geophysics, Geosystems, v. 14, p. 3315–3323, doi:10.1002/ggge.20193.

740 Ghisetti, F.C., Barnes, P.M., Ellis, S., Plaza-Faverola, A.A., and Barker, D.H.N., 2016, The last 2 Myr
741 of accretionary wedge construction in the central Hikurangi margin (North Island, New
742 Zealand): Insights from structural modeling: Geochemistry, Geophysics, Geosystems, v. 17, p.
743 2661–2686, doi:10.1002/2016GC006341.

744 Ghosal, D., Singh, S.C., and Martin, J., 2014, Shallow subsurface morphotectonics of the NW
745 Sumatra subduction system using an integrated seismic imaging technique: Geophysical Journal
746 International, v. 198, p. 1818–1831, doi:10.1093/gji/ggu182.

747 Goto, S., and Matsubayashi, O., 2009, Relations between the thermal properties and porosity of
748 sediments in the eastern flank of the Juan de Fuca Ridge: Earth, Planets and Space, v. 61, p.
749 863–870, doi:10.1186/BF03353197.

750 Graetsch, H., 1994, Structural characteristics of opaline and microcrystalline silica minerals. In Silica:
751 Reviews in mineralogy, v. 29, p. 209–232.

752 Gulick, S.P.S., Austin, J.A., McNeill, L.C., Bangs, N.L.B., Martin, K.M., Henstock, T.J., Bull, J.M.,
753 Dean, S., Djajadihardja, Y.S., and Permana, H., 2011, Updip rupture of the 2004 Sumatra
754 earthquake extended by thick indurated sediments: Nature Geoscience, v. 4, p. 453–456,
755 doi:10.1038/ngeo1176.

756 Gutscher, M.A., Klaeschen, D., Flueh, E., and Malavieille, J., 2001, Non-Coulomb wedges, wrong-
757 way thrusting, and natural hazards in Cascadia: Geology, v. 29, p. 379–382, doi:10.1130/0091-
758 7613(2001)029<0379:NCWWWT>2.0.CO;2.

759 Gutscher, M.A., Klingelhoefer, F., Theunissen, T., Spakman, W., Berthet, T., Wang, T.K., and Lee,
760 C.S., 2016, Thermal modeling of the SW Ryukyu forearc (Taiwan): Implications for the
761 seismogenic zone and the age of the subducting Philippine Sea Plate (Huatung Basin):
762 Tectonophysics, v. 692, p. 131–142, doi:10.1016/j.tecto.2016.03.029.

763 Han, S., Bangs, N.L., Carbotte, S.M., Saffer, D.M., and Gibson, J.C., 2017, Links between sediment
764 consolidation and Cascadia megathrust slip behaviour: Nature Geoscience, v. 10, p. 954–959,
765 doi:10.1038/s41561-017-0007-2.

766 Harris, R.N., Spinelli, G.A., and Hutnak, M., 2020, Heat Flow Evidence for Hydrothermal Circulation
767 in Oceanic Crust Offshore Grays Harbor, Washington: Geochemistry, Geophysics, Geosystems,
768 v. 21, doi:10.1029/2019GC008879.

769 Hippchen, S., and Hyndman, R.D., 2008, Thermal and structural models of the Sumatra subduction
770 zone: Implications for the megathrust seismogenic zone: Journal of Geophysical Research: Solid
771 Earth, v. 113, p. 1–12, doi:10.1029/2008JB005698.

772 Housen, B.A. et al., 1996, Strain decoupling across the decollement of the Barbados accretionary
773 prism: Geology, v. 24, p. 127–130, doi:10.1130/0091-
774 7613(1996)024<0127:SDATDO>2.3.CO;2.

775 Huang, W.-L., Longo, J.M., and Pevear, D.R., 1993, An experimentally derived kinetic model for
776 smectite-to-illite conversion and its use as a geothermometer: Clays and Clay Minerals, v. 41, p.
777 162–177.

778 Hüpers, A. et al., 2017, Release of mineral-bound water prior to subduction tied to shallow
779 seismogenic slip off Sumatra: Science, v. 356, p. 841–844, doi:10.1126/science.aal3429.

780 Hutchison, I., 1985, The effects of sedimentation and compaction on oceanic heat flow: Geophysical
781 Journal of the Royal Astronomical Society, v. 82, p. 439–459, doi:10.1111/j.1365-
782 246X.1985.tb05145.x.

783 Hutnak, M., and Fisher, A.T., 2007, Influence of sedimentation, local and regional hydrothermal
784 circulation, and thermal rebound on measurements of seafloor heat flux: Journal of Geophysical
785 Research: Solid Earth, v. 112, p. 1–19, doi:10.1029/2007JB005022.

786 Hyndman, R.D., and Wang, K., 1993, Thermal Constraints on the Zone of Major Thrust Earthquake
787 Failure: The Cascadia Subduction Zone: Journal of Geophysical Research, v. 98, p. 2039–2060.

788 Hyndman, R.D., Wang, K., and Yamano, M., 1995, Thermal constraints on the seismogenic portion of
789 the southwestern Japan subduction thrust: Journal of Geophysical Research: Solid Earth, v. 100,
790 p. 15373–15392.

791 Hyndman, R.D., Wang, K., Yuan, T., and Spence, G.D., 1993, Tectonic sediment thickening, fluid
792 expulsion, and the thermal regime of subduction zone accretionary prisms: the Cascadia margin
793 off Vancouver Island: Journal of Geophysical Research, v. 98, doi:10.1029/93jb02391.

794 Hyndman, R.D., Yamano, M., and Oleskevich, D.A., 1997, The seismogenic zone of subduction
795 thrust faults: Island Arc, v. 6, p. 244–260, doi:10.1111/j.1440-1738.1997.tb00175.x.

796 Ikari, M.J., Saffer, D.M., and Marone, C., 2007, Effect of hydration state on the frictional properties
797 of montmorillonite-based fault gouge: Journal of Geophysical Research: Solid Earth, v. 112, p.

798 1–12, doi:10.1029/2006JB004748.

799 Ike, T., Moore, G.F., Kuramoto, S., Park, J.O., Kaneda, Y., and Taira, A., 2008, Variations in
800 sediment thickness and type along the northern Philippine Sea Plate at the Nankai Trough:
801 Island Arc, v. 17, p. 342–357, doi:10.1111/j.1440-1738.2008.00624.x.

802 Jacob, J., Dyment, J., and Yatheesh, V., 2014, Revisiting the structure, age, and evolution of the
803 Wharton Basin to better understand subduction under Indonesia: Journal of Geophysical
804 Research: Solid Earth, v. 119, p. 169–190, doi:10.1002/2013JB010285.

805 Jessop, A.M., 2012, The world heat flow data collection-1975:

806 Kimura, G., Hina, S., Hamada, Y., Kameda, J., Tsuji, T., Kinoshita, M., and Yamaguchi, A., 2012,
807 Runaway slip to the trench due to rupture of highly pressurized megathrust beneath the middle
808 trench slope: The tsunamigenesis of the 2011 Tohoku earthquake off the east coast of northern
809 Japan: Earth and Planetary Science Letters, v. 339–340, p. 32–45,
810 doi:10.1016/j.epsl.2012.04.002.

811 Klingelhoefer, F., Gutscher, M.A., Ladage, S., Dessa, J.X., Graindorge, D., Franke, D., André, C.,
812 Permana, H., Yudistira, T., and Chauhan, A., 2010, Limits of the seismogenic zone in the
813 epicentral region of the 26 December 2004 great Sumatra-Andaman earthquake: Results from
814 seismic refraction and wide-angle reflection surveys and thermal modeling: Journal of
815 Geophysical Research: Solid Earth, v. 115, p. 1–23, doi:10.1029/2009JB006569.

816 Lay, T. et al., 2005, The great Sumatra-Andaman earthquake of 26 December 2004: Science, v. 308,
817 p. 1127–1133, doi:10.1126/science.1112250.

818 Lockner, D.A., and Byerlee, J., 1986, Laboratory measurements of velocity-dependent frictional
819 strength: USGS Open File Report 86-417, p. 55, doi:10.3133/ofr86417.

820 Lovell, M.A., 1985, Thermal conductivities of marine sediments.: Quarterly Journal of Engineering
821 Geology, v. 18, p. 437–441.

822 MacKay, M.E., 1995, Structural variation and landward vergence at the toe of the Oregon
823 accretionary prism: Tectonics, v. 14, p. 1309–1320, doi:10.1029/95TC02320.

824 MacKay, M.E., Moore, G.F., Cochrane, G.R., Casey Moore, J., and Kulm, L.V.D., 1992, Landward
825 vergence and oblique structural trends in the Oregon margin accretionary prism: Implications
826 and effect on fluid flow: Earth and Planetary Science Letters, v. 109, p. 477–491,
827 doi:10.1016/0012-821X(92)90108-8.

828 Marone, C., and Scholz, C.H., 1988, The depth of seismic faulting and the upper transition from
829 stable to unstable slip regimes: Geophysical Research Letters, v. 15, p. 621–624,

830 doi:10.1029/GL015i006p00621.

831 McKenzie, D., Jackson, J., and Priestley, K., 2005, Thermal structure of oceanic and continental
832 lithosphere: Earth and Planetary Science Letters, v. 233, p. 337–349,
833 doi:10.1016/j.epsl.2005.02.005.

834 McNeill, L.C. et al., 2017, Expedition 362 summary: Proceedings of the International Ocean
835 Discovery Program, v. 362, p. 21–22, doi:10.7289/V5C8276M.

836 McNeill, L.C., 2017, Expedition 362 summary (B. Dugan et al., Eds.): - Proceedings of the
837 International Ocean Discovery Program; Sumatra subduction zone; Expedition 362 of the
838 riserless drilling platform, Colombo, Sri Lanka, to Singapore; Sites U1480-U1481, 6 August-6
839 October 2016, v. 362, p. 20, http://hdl.handle.net/10.14379/iodp.proc.362.101.2017.

840 McNeill, L.C., and Henstock, T.J., 2014, Forearc structure andmorphology along the Sumatra-
841 Andaman subduction zone: Tectonics, v. 33, p. 112–134, doi:10.1002/2012tc003264.

842 Mizutani, S., 1970, Silica Minerals in the Early Stage of Diagenesis: Sedimentology, v. 15, p. 419–
843 436, doi:10.1111/j.1365-3091.1970.tb02193.x.

844 Moore, J.C., 1982, Offscraping and underthrusting of sediment at the deformation front of the
845 Barbados Ridge: Deep Sea Drilling Project Leg 78A.: Geological Society of America Bulletin,
846 v. 93, p. 1065–1077, doi:10.1130/0016-7606(1982)93<1065:OAUOSA>2.0.CO;2.

847 Moore, J.C., Rowe, C., and Meneghini, F., 2007, MHow Accretionary Prisms Elucidate
848 Seismogenesis in Subduction Zones: The seismogenic zone of subduction thrust faults, p. 288.

849 Moore, J.C., and Saffer, D., 2001, Updip limit of the seismogenic zone beneath the accretionary prism
850 of Southwest Japan: An effect of diagenetic to low-grade metamorphic processes and increasing
851 effective stress: Geology, v. 29, p. 183–186, doi:10.1130/0091-
852 7613(2001)029<0183:ULOTSZ>2.0.CO;2.

853 Müller, R.D., Sdrolias, M., Gaina, C., and Roest, W.R., 2008, Age, spreading rates, and spreading
854 asymmetry of the world's ocean crust: Geochemistry, Geophysics, Geosystems, v. 9,
855 doi:10.1029/2007GC001743.

856 Olsen, K.M., Bangs, N.L., Tréhu, A.M., Han, S., Arnulf, A., and Contreras-Reyes, E., 2020, Thick,
857 strong sediment subduction along south-central Chile and its role in great earthquakes: Earth and
858 Planetary Science Letters, v. 538, doi:10.1016/j.epsl.2020.116195.

859 Pickering, K.T. et al., 2020, Sedimentology, stratigraphy and architecture of the Nicobar Fan
860 (Bengal–Nicobar Fan System), Indian Ocean: Results from International Ocean Discovery
861 Program Expedition 362: Sedimentology, doi:10.1111/sed.12701.

862 Pytte, A.M., and Reynolds, R.C., 1989, The thermal transformation of smectite to illite, *in* Thermal
863 history of sedimentary basins, Springer, p. 133–140.

864 Qin, Y., and Singh, S.C., 2017, Detailed seismic velocity of the incoming subducting sediments in the
865 2004 great Sumatra earthquake rupture zone from full waveform inversion of long offset seismic
866 data: Geophysical Research Letters, v. 44, p. 3090–3099, doi:10.1002/2016GL072175.

867 Rabinowicz, E., 1958, The intrinsic variables affecting the stick-slip process: Proceedings of the
868 Physical Society, v. 71, p. 668–675, doi:10.1088/0370-1328/71/4/316.

869 Ranero, C.R., Grevemeyer, I., Sahling, H., Barckhausen, U., Hensen, C., Wallmann, K., Weinrebe,
870 W., Vannucchi, P., Von Huene, R., and McIntosh, K., 2008, Hydrogeological system of
871 erosional convergent margins and its influence on tectonics and interplate seismogenesis:
872 Geochemistry, Geophysics, Geosystems, v. 9, doi:10.1029/2007GC001679.

873 Rosenberger, K., Underwood, M.B., Vrolijk, P., and Haines, S., 2020, Data report: clay mineral
874 assemblages in hemipelagic sediments entering the Sumatra subduction zone, IODP Sites U1480
875 and U1481, Expedition 362.: Proceedings of the International Ocean Discovery Program, 362:
876 College Station, TX (International Ocean Discovery Program).,
877 doi:10.14379/iodp.proc.362.204.2020.

878 Rybach, L., 1986, Amount and significance of radioactive heat sources in sediments: Collection
879 colloques seminares, v. 44, p. 311–322.

880 Saffer, D.M., Lockner, D.A., and McKiernan, A., 2012, Effects of smectite to illite transformation on
881 the frictional strength and sliding stability of intact marine mudstones: Geophysical Research
882 Letters, v. 39, doi:10.1029/2012GL051761.

883 Saffer, D.M., and McKiernan, A.W., 2009, Evaluation of in situ smectite dehydration as a pore water
884 freshening mechanism in the nankai trough, offshore southwest Japan: Geochemistry,
885 Geophysics, Geosystems, v. 10, doi:10.1029/2008GC002226.

886 Saffer, D.M., and Tobin, H.J., 2011, Hydrogeology and Mechanics of Subduction Zone Forearcs:
887 Fluid Flow and Pore Pressure: Annual Review of Earth and Planetary Sciences, v. 39, p. 157–
888 186, doi:10.1146/annurev-earth-040610-133408.

889 Saffer, D.M., Underwood, M.B., and Mckiernan, A.W., 2008, Evaluation of factors controlling
890 smectite transformation and fluid production in subduction zones: Application to the Nankai
891 Trough: Island Arc, v. 17, p. 208–230, doi:10.1111/j.1440-1738.2008.00614.x.

892 Salmi, M.S., Johnson, H.P., and Harris, R.N., 2017, Thermal environment of the Southern
893 Washington region of the Cascadia subduction zone: Journal of Geophysical Research: Solid

894 Earth, v. 122, p. 5852–5870, doi:10.1002/2016JB013839.

895 Scholz, C.H., 1998, Earthquakes and friction laws: Nature, v. 391, p. 37–42, doi:10.1038/34097.

896 Scholz, C.H., 2019, The mechanics of earthquakes and faulting: Cambridge university press.

897 Simons, M. et al., 2011, The 2011 magnitude 9.0 Tohoku-Oki earthquake: Mosaicking the megathrust
898 from seconds to centuries: Science, v. 332, p. 1421–1425, doi:10.1126/science.1206731.

899 Singh, S.C., Chauhan, A.P.S., Calvert, A.J., Hananto, N.D., Ghosal, D., Rai, A., and Carton, H., 2012,
900 Seismic evidence of bending and unbending of subducting oceanic crust and the presence of
901 mantle megathrust in the 2004 Great Sumatra earthquake rupture zone: Earth and Planetary
902 Science Letters, v. 321–322, p. 166–176, doi:10.1016/j.epsl.2012.01.012.

903 Smith, G., McNeill, L., Henstock, I.J., and Bull, J., 2012, The structure and fault activity of the
904 Makran accretionary prism: Journal of Geophysical Research: Solid Earth, v. 117, p. 1–17,
905 doi:10.1029/2012JB009312.

906 Smith, G.L., McNeill, L.C., Wang, K., He, J., and Henstock, T.J., 2013, Thermal structure and
907 megathrust seismogenic potential of the Makran subduction zone: Geophysical Research Letters,
908 v. 40, p. 1528–1533, doi:10.1002/grl.50374.

909 Spinelli, G.A., and Saffer, D.M., 2004, Along-strike variations in underthrust sediment dewatering on
910 the Nicoya margin, Costa Rica related to the updip limit of seismicity: Geophysical Research
911 Letters, v. 31, p. 1–5, doi:10.1029/2003GL018863.

912 Spinelli, G.A., and Underwood, M.B., 2004, Character of sediments entering the Costa Rica
913 subduction zone: Implications for partitioning of water along the plate interface: Island Arc, v.
914 13, p. 432–451, doi:10.1111/j.1440-1738.2004.00436.x.

915 Stein, C.A., and Abbott, D.H., 1991, Heat Flow Constraints on the South Pacific Superswell Lamont-
916 Doherty Geological Observatory, Palisades, New York: Journal of Geophysical Research, v.
917 96099, p. 83–16, doi:10.1029/91JB00774.

918 Stein, C.A., and Stein, S., 1992, a Model for the Global Variation in Oceanic Depth and Heat-Flow
919 With Lithospheric Age: Nature, v. 359, p. 123–129, doi:10.1038/359123a0.

920 Stevens, D.E., McNeill, L.C., Henstock, T.J., Delescluse, M., Chamot-Rooke, N., and Bull, J.M.,
921 2020, A complete structural model and kinematic history for distributed deformation in the
922 Wharton Basin: Earth and Planetary Science Letters, v. 538, doi:10.1016/j.epsl.2020.116218.

923 Tappin, D.R., McNeil, L.C., Henstock, T., and Mosher, D.C., 2007, Mass wasting processes-offshore
924 Sumatra, *in* Submarine mass movements and their consequences, Springer, p. 327–336.

925 Underwood, M.B., 2007, Sediment inputs to subduction zones: Why lithostratigraphy and clay
926 mineralogy matter: The seismogenic zone of subduction thrust faults,.

927 Vrolijk, P., 1990, On the mechanical role of smectite in subduction zones: Geology, v. 18, p. 703–
928 707, doi:10.1130/0091-7613(1990)018<0703:OTMROS>2.3.CO;2.

929 Wang, K., and Hu, Y., 2006, Accretionary prisms in subduction earthquake cycles: The theory of
930 dynamic Coulomb wedge: Journal of Geophysical Research: Solid Earth, v. 111, p. 1–16,
931 doi:10.1029/2005JB004094.

932 Wells, R.E., 2003, Correction to "Basin-centered asperities in great subduction zone earthquakes: A
933 link between slip, subsidence, and subduction erosion?" Journal of Geophysical Research, v.
934 108, p. 2562, doi:10.1029/2003JB002880.

935 Westbrook, G.K., and Reston, T.J., 2002, The accretionary complex of the Mediterranean Ridge:
936 Tectonics, fluid flow and the formation of brine lakes - An introduction to the special issue of
937 Marine Geology: Marine Geology, v. 186, p. 1–8, doi:10.1016/S0025-3227(02)00169-X.

938

939

940 ## 8 Figure Captions

941 **Figure 1.** Regional tectonics, plate age and seafloor heat flux. A) Eastern Indian Ocean setting.
942 Toothed line is Sumatra-Andaman subduction zone deformation front; bathymetry (2000 m contours)
943 with Ninety East Ridge (NER); red box, location of (B). B) Age contours of oceanic crust (Jacob et
944 al., 2014); red-white-blue points, seafloor heat flux measurements from Jessop (2012) in mWm^{-2};
945 brown squares IODP sites, orange diamond and associated value show average surface heat flow at
946 site U1480 calculated by IODP in mWm^{-2}; black lines (1 and 2) are seismic profiles. SSZ – Sumatra
947 subduction zone. C) Predicted basal heat flux from Stein and Stein (1992) model for cooling of
948 oceanic crust (without any sedimentation efftects), with surface heat flux points from (B). Heat flux
949 measurement colours indicate measured value relative to predicted value for plate age at site (of Stein
950 and Stein, 1992); red=high; blue=low; white=close to predicted value.

951 **Figure 2.** Interpretation of seismic profile 1, with Site U1480, reflectors R1-14 used for modelling,
952 and major lithostratigraphic units. Note substantial increase in thickness of Unit A towards
953 deformation front.

954 **Figure 3.** Age information at Site U1480 and extrapolation to deformation front (DF). A) Age model
955 for Site U1480 based on biostratigraphic tie points (Backman et al., 2019) and interpolated ages of
956 reflectors R1 – R11 (extant at the drill site). R12 has interpolated age of 14.4 Ma; an age cannot be

reliably defined for R13; R14 is top of oceanic basement (~68 Ma). B) Extrapolated age model for location at deformation front. Itallic numbers in (A) and (B) are sediment accumulation rates in m/Myr, bold itallic numbers = average sediment accumulation rates for each unit. C) Lower stratigraphic units at Site U1480, showing igneous intervals units; sediments overlying shallowest interval in Unit IV ~58 Ma.

Figure 4. Natural Gamma Ray logging data for uncased intervals of sites U1480 and U1481 and conversion to radiogenic heat production based on method of Bücker and Rybach (1996).

Figure 5. Burial history, thermal evolution and fluid release rate at reflector R11 (solid lines) and top basement (dashed lines) at Site U1480, Pseudo site 1 and Pseudo Site 2, over last 10 Myr (deposition of Nicobar Fan and trench wedge). A-C) Burial depth, porosity reduction and temperature change. D-F) Change in molar fraction of hydrated mineral forms, opal and smectite. G-I) Dehydration fluid expulsion rate (unit volume s^{-1}) from : compaction (porosity reduction); silica dehydration (Opal-Quartz transformation) and smectite dehydration (smectite-illite transformation). Grey shaded area indicates time when trench wedge is developed (at Site U1480, trench wedge is not well developed).

Figure 6. Thermal structure evolution of the incoming sediment column across seismic profile 1, and corresponding modelled seafloor heat flux. A) Seafloor heat flux model output at discrete time steps. Orange shaded area is zone where thermal rejuvenation was applied at 58 Ma. B-E) Thermal structure of sediment column through time. Solid lines are reflectors used in grid creation, dashed lines are positions of remaining reflectors for reference. PD = present day.

Figure 7. Smectite dehydration state of the incoming sediment column across seismic profile 1, and corresponding fluid thickness generated based on the Pytte and Reynolds (1989) kinetic. A) Along-profile fluid thickness from sediments underlying reflector R11 (dashed line in B-E) over discrete time steps and total. B-E) Instantaneous fluid production rate at specific timings. PD = present day.

Figure 8. Cumulative total fluid expelled from sediments underlying reflector R11 along seismic profile 1 broken down into constituent sources. A) Amorphous silica dehydration B) Compaction (porosity-loss). C and D) Smectite dehydration as modelled by the Huang et al. (1993) and Pytte and Reynolds (1989) equations, respectively. E) Cumulative total, also showing temperatures at reflector R11 from 2.2 Ma.

Word Count: 9470; fig captions 614, text 8856

Figure 1.

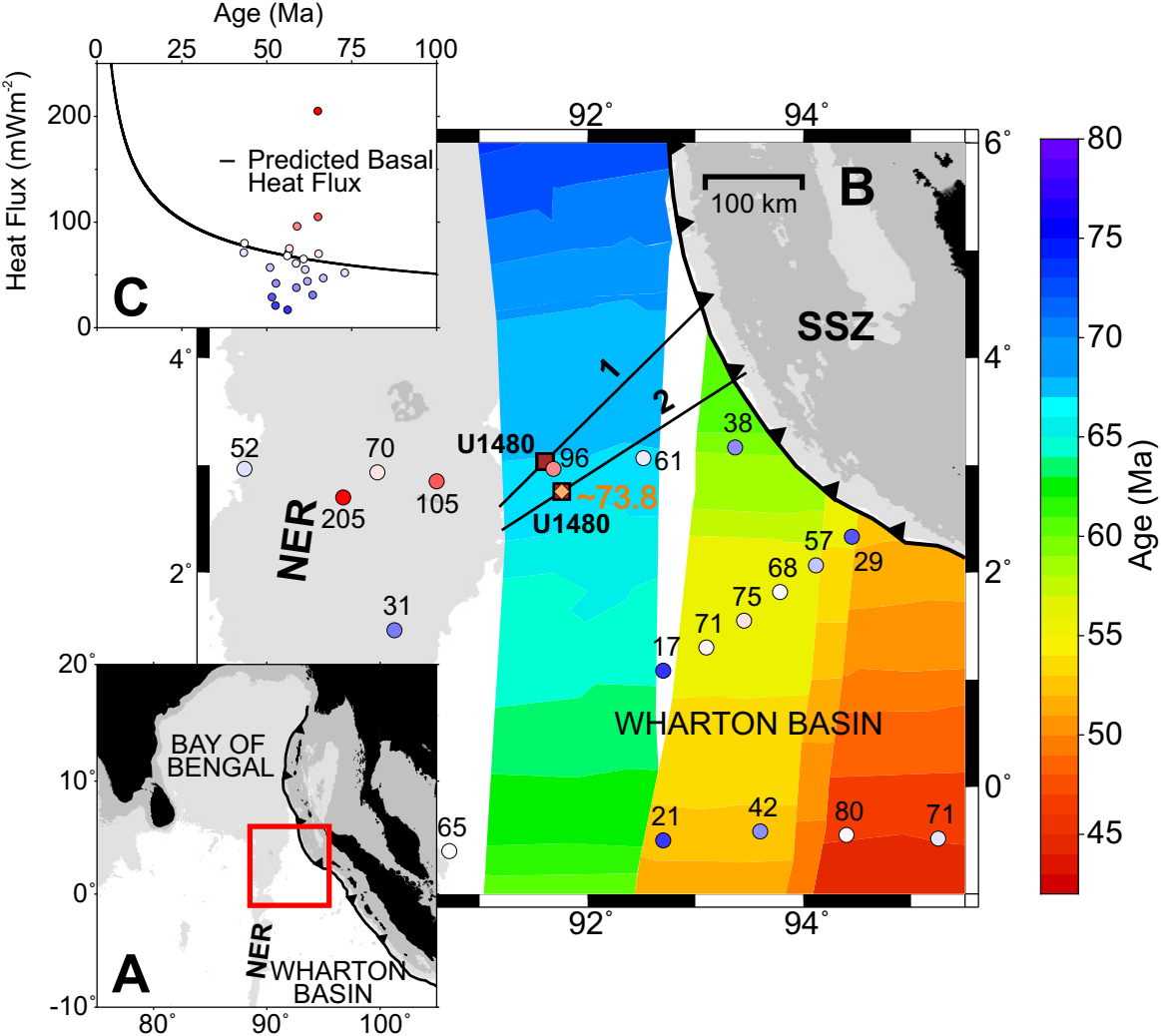
Age (Ma)
0
25
50
75
100
Heat Flux (mWm-2)
200
100
0
Predicted Basal Heat Flux
C
92˚
94˚
6˚
4˚
2˚
0˚
100 km
B
SSZ
1
2
U1480
96
61
~73.8
U1480
38
52
70
105
205
NER
31
57
29
68
75
71
17
WHARTON BASIN
21
42
80
71
65
20˚
10˚
0˚
-10˚
80˚
90˚
100˚
BAY OF BENGAL
A
NER
WHARTON BASIN
80
75
70
65
60
55
50
45
Age (Ma)

Figure 2.

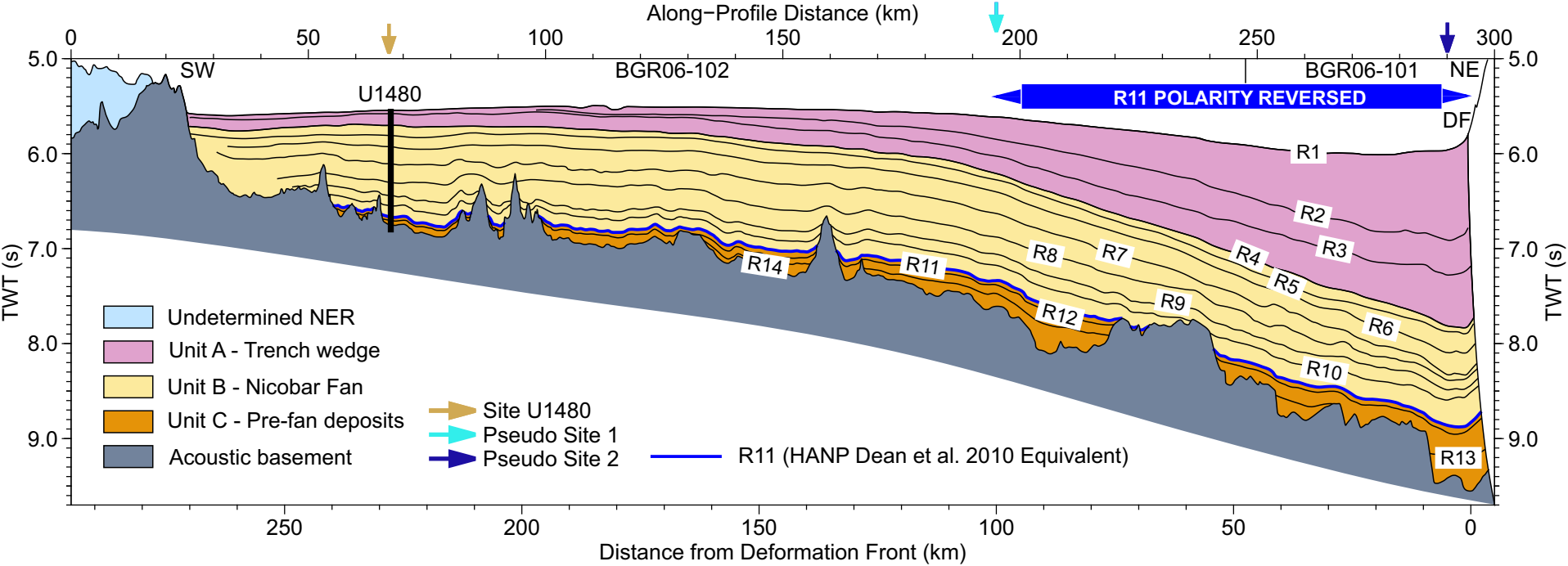
Along−Profile Distance (km)
0
50
100
150
200
250
300
SW
U1480
BGR06-102
BGR06-101
NE
R11 POLARITY REVERSED
DF
R1
R2
R3
R4
R5
R6
R7
R8
R9
R10
R11
R12
R13
R14
TWT (s)
5.0
6.0
7.0
8.0
9.0
Undetermined NER
Unit A - Trench wedge
Unit B - Nicobar Fan
Unit C - Pre-fan deposits
Acoustic basement
Site U1480
Pseudo Site 1
Pseudo Site 2
R11 (HANP Dean et al. 2010 Equivalent)
Distance from Deformation Front (km)

Figure 3.

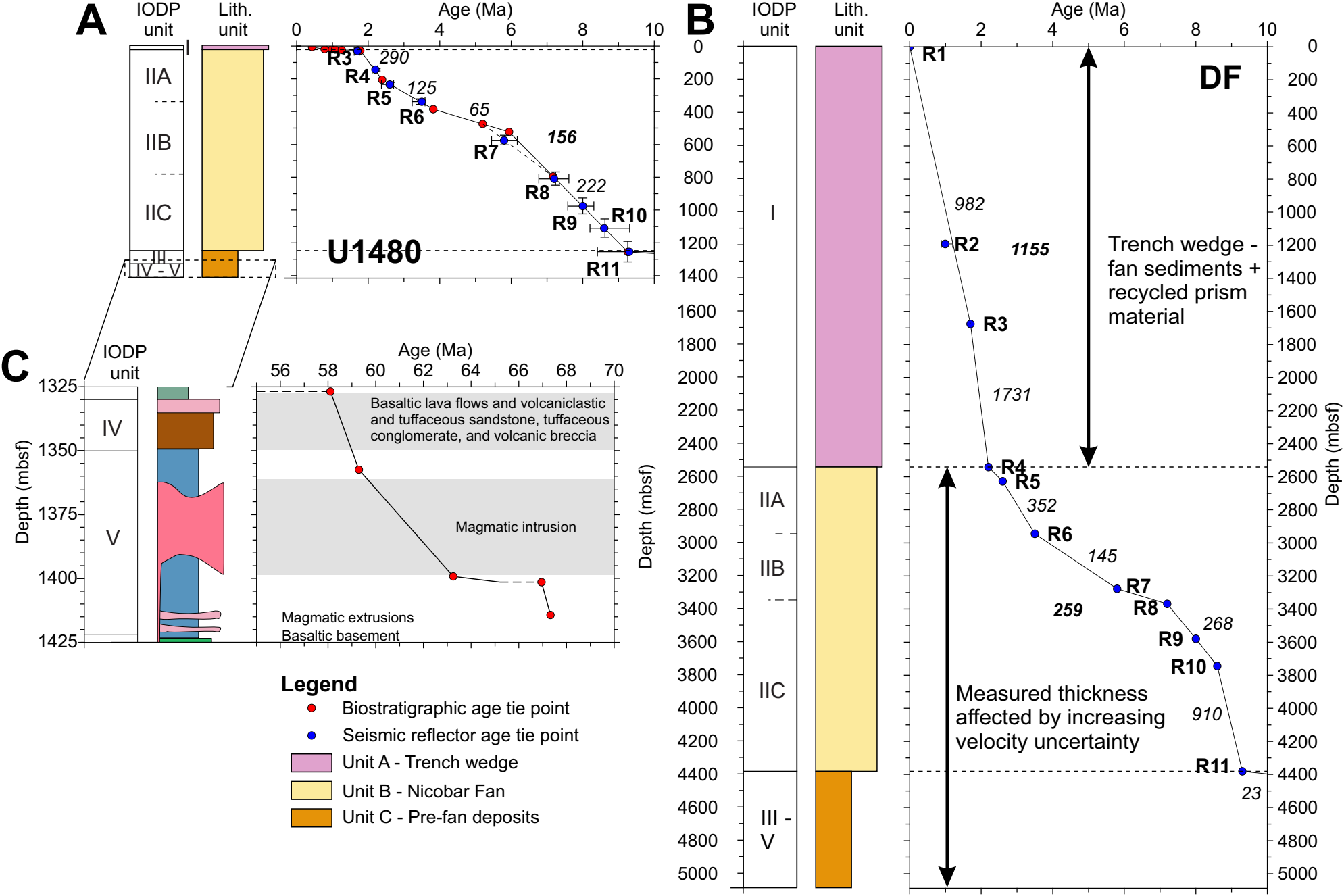
A
IODP unit
Lith. unit
Age (Ma)
IIA
IIB
IIC
III
IV - V
U1480
R3
R4
R5
R6
R7
R8
R9
R10
R11
290
125
65
156
222
B
I
IIA
IIB
IIC
III - V
DF
R1
R2
R3
R4
R5
R6
R7
R8
R9
R10
R11
982
1155
1731
352
145
259
268
910
23
Trench wedge - fan sediments + recycled prism material
Measured thickness affected by increasing velocity uncertainty
Depth (mbsf)
C
IV
V
Basaltic lava flows and volcaniclastic and tuffaceous sandstone, tuffaceous conglomerate, and volcanic breccia
Magmatic intrusion
Magmatic extrusions
Basaltic basement
Legend
Biostratigraphic age tie point
Seismic reflector age tie point
Unit A - Trench wedge
Unit B - Nicobar Fan
Unit C - Pre-fan deposits

Figure 4.

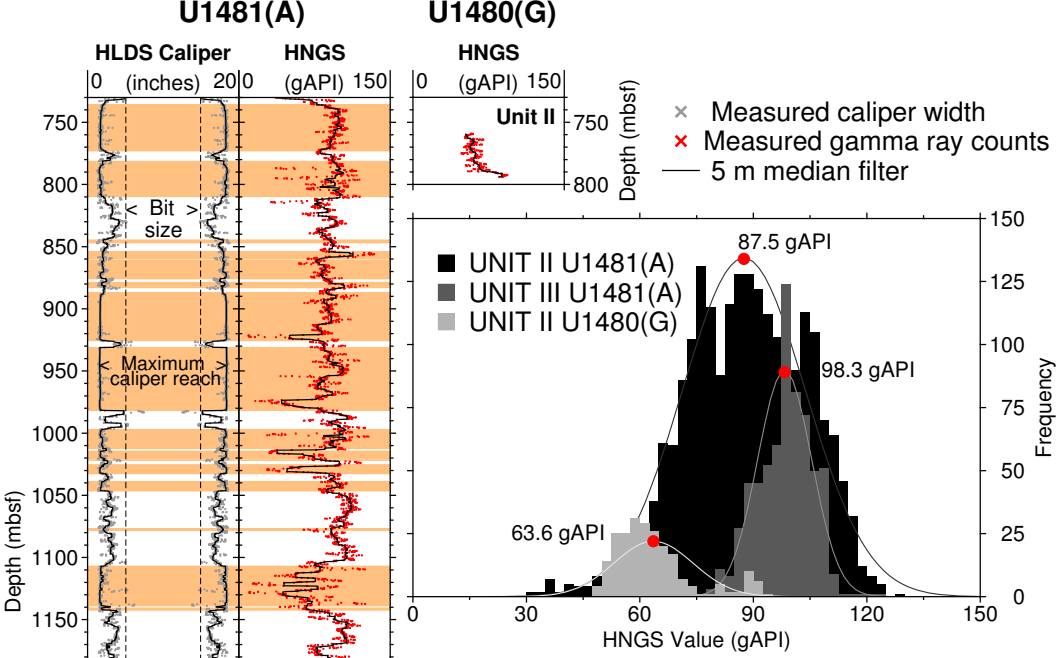

From Bücker and Ryback 1996, Radiogenic heat production **A[μW/m^3] = 0.0158(GR[gAPI] - 0.8)**

	Mean gAPI	A[μW/m^3]
UNIT II U1481(A)	87.5	1.37
UNIT II U1480(G)	63.6	0.99
UNIT III U1481(A)	98.3	1.54

Figure 5.

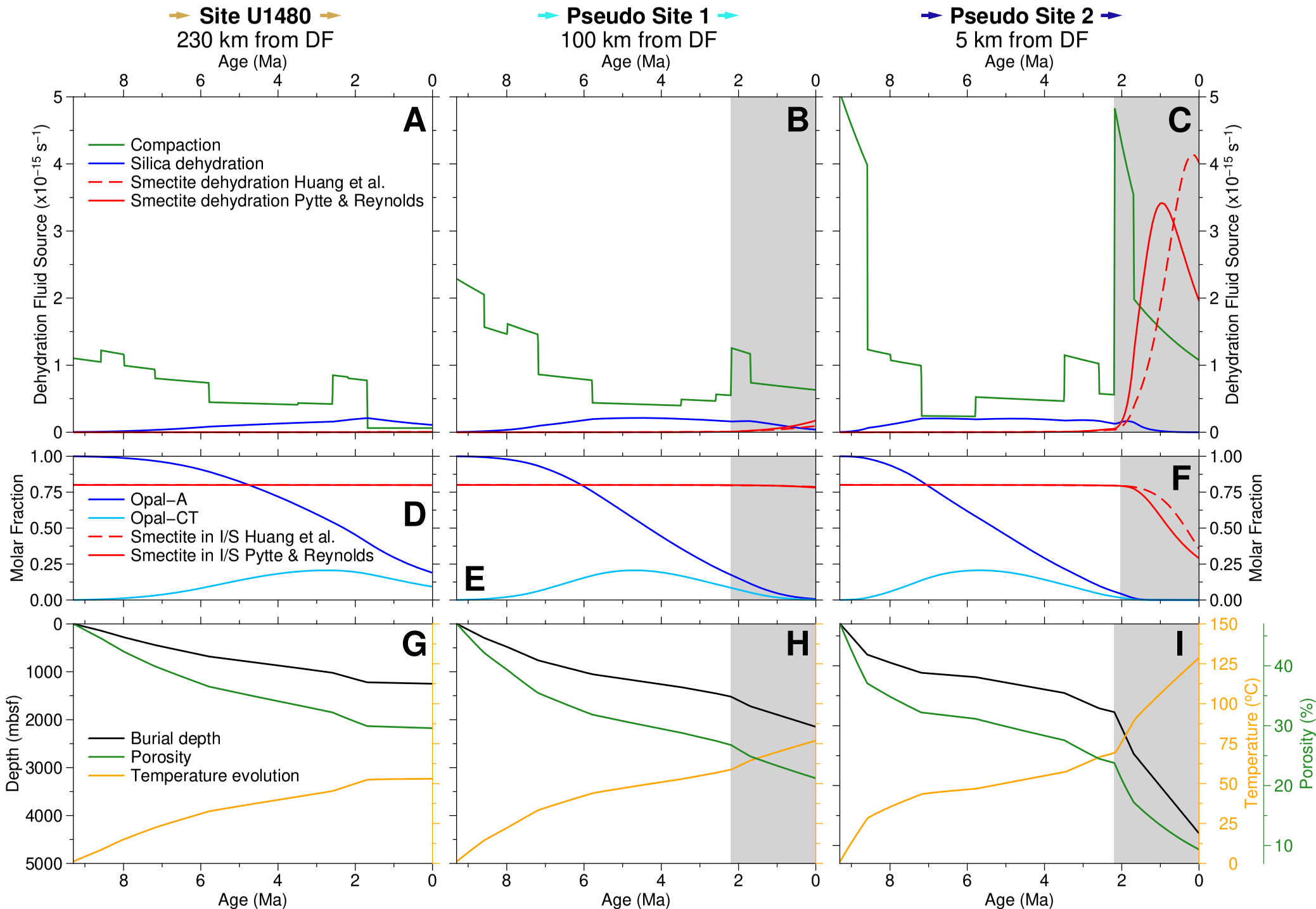
Site U1480
230 km from DF
Pseudo Site 1
100 km from DF
Pseudo Site 2
5 km from DF
Age (Ma)
A
B
C
D
E
F
G
H
I
Compaction
Silica dehydration
Smectite dehydration Huang et al.
Smectite dehydration Pytte & Reynolds
Dehydration Fluid Source (x10⁻¹⁵ s⁻¹)
Opal–A
Opal–CT
Smectite in I/S Huang et al.
Smectite in I/S Pytte & Reynolds
Molar Fraction
Burial depth
Porosity
Temperature evolution
Depth (mbsf)
Temperature (°C)
Porosity (%)

Figure 6.

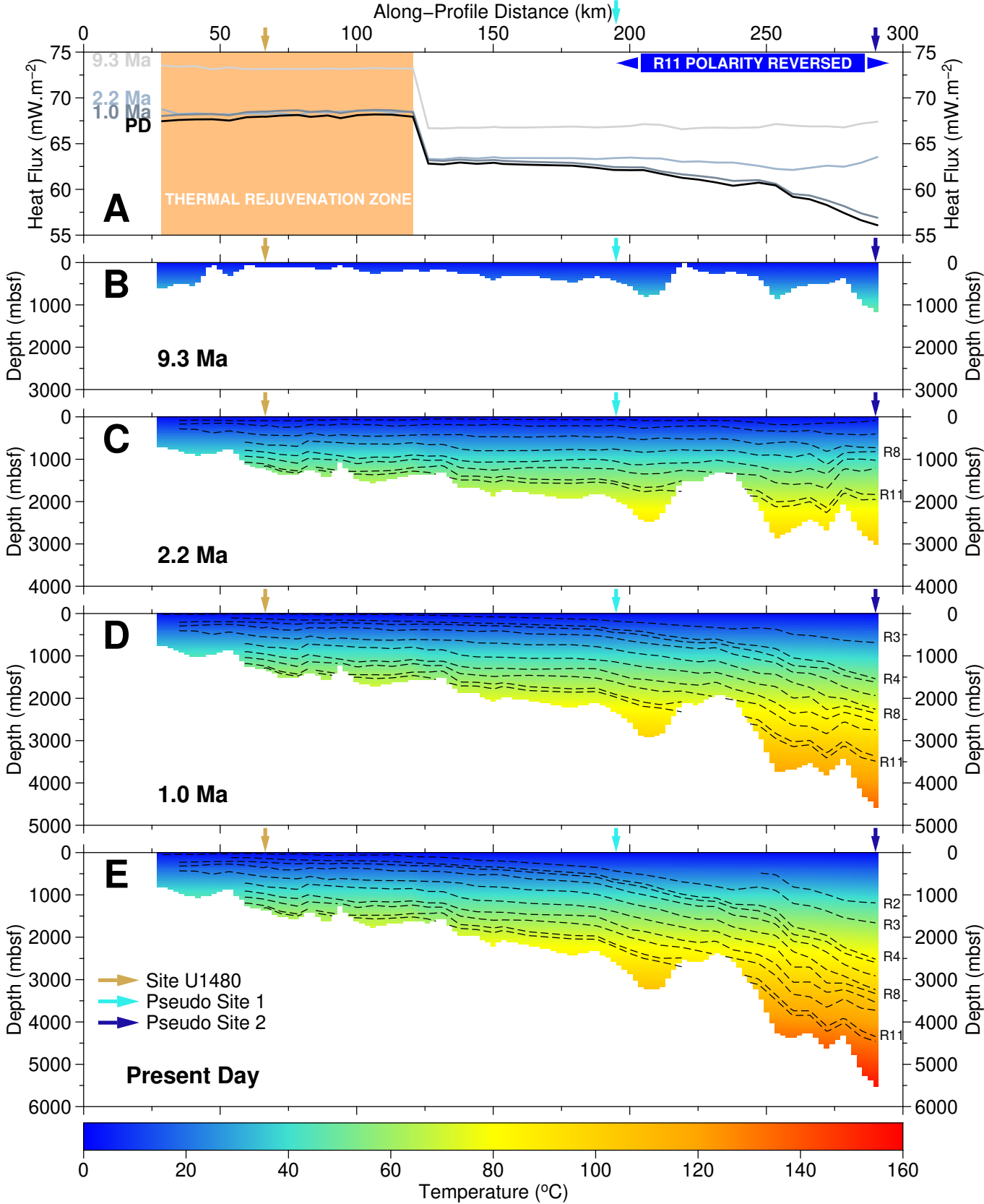
Along−Profile Distance (km)
0
50
100
150
200
250
300
A
Heat Flux (mW.m^{-2})
9.3 Ma
2.2 Ma
1.0 Ma
PD
R11 POLARITY REVERSED
THERMAL REJUVENATION ZONE
B
Depth (mbsf)
9.3 Ma
C
2.2 Ma
R8
R11
D
1.0 Ma
R3
R4
R8
R11
E
Present Day
R2
R3
R4
R8
R11
Site U1480
Pseudo Site 1
Pseudo Site 2
Temperature (°C)

Figure 7.

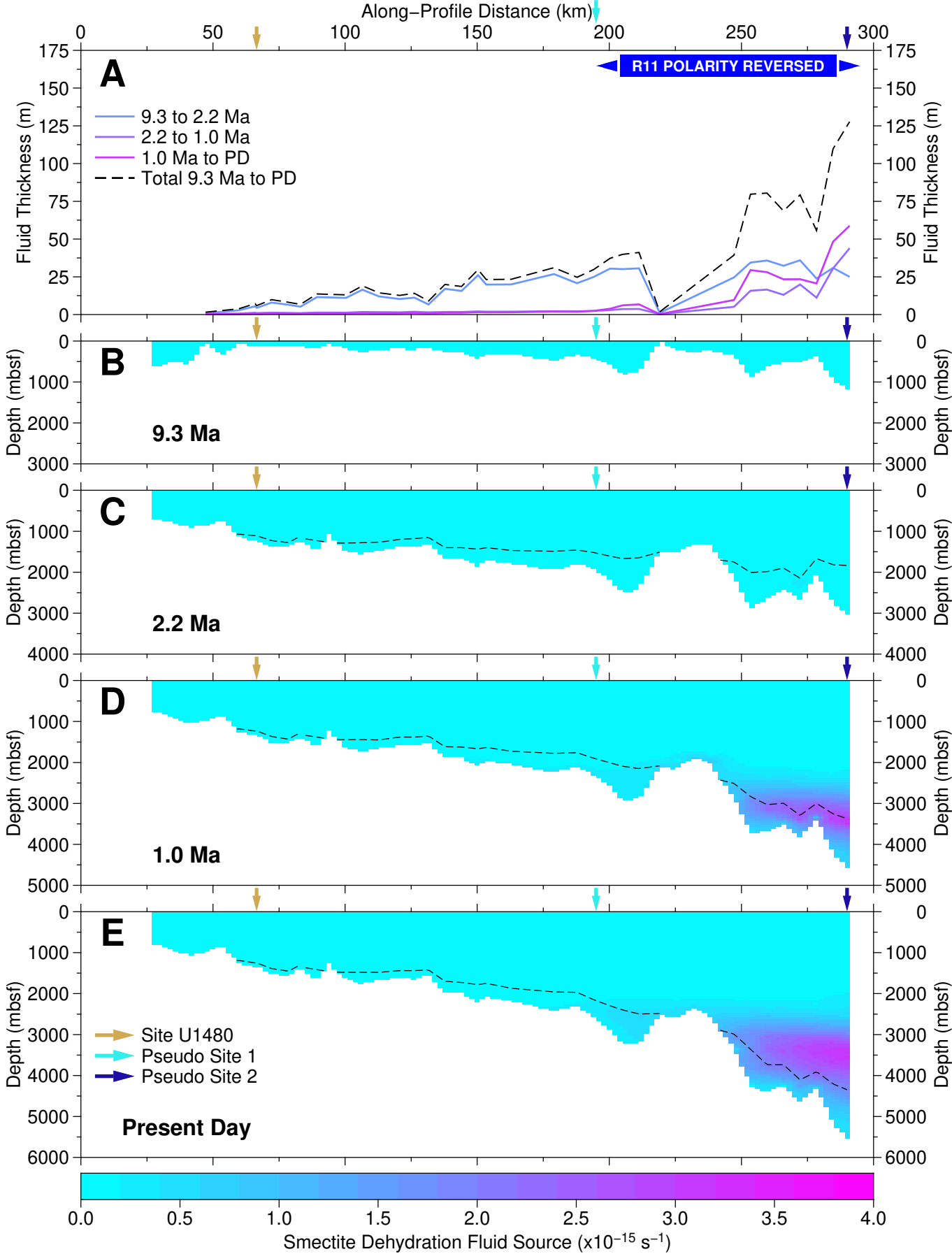
Along−Profile Distance (km)
0
50
100
150
200
250
300
A
R11 POLARITY REVERSED
9.3 to 2.2 Ma
2.2 to 1.0 Ma
1.0 Ma to PD
Total 9.3 Ma to PD
Fluid Thickness (m)
B
9.3 Ma
C
2.2 Ma
D
1.0 Ma
E
Present Day
Depth (mbsf)
Site U1480
Pseudo Site 1
Pseudo Site 2
Smectite Dehydration Fluid Source (x10−15 s−1)

Figure 8.

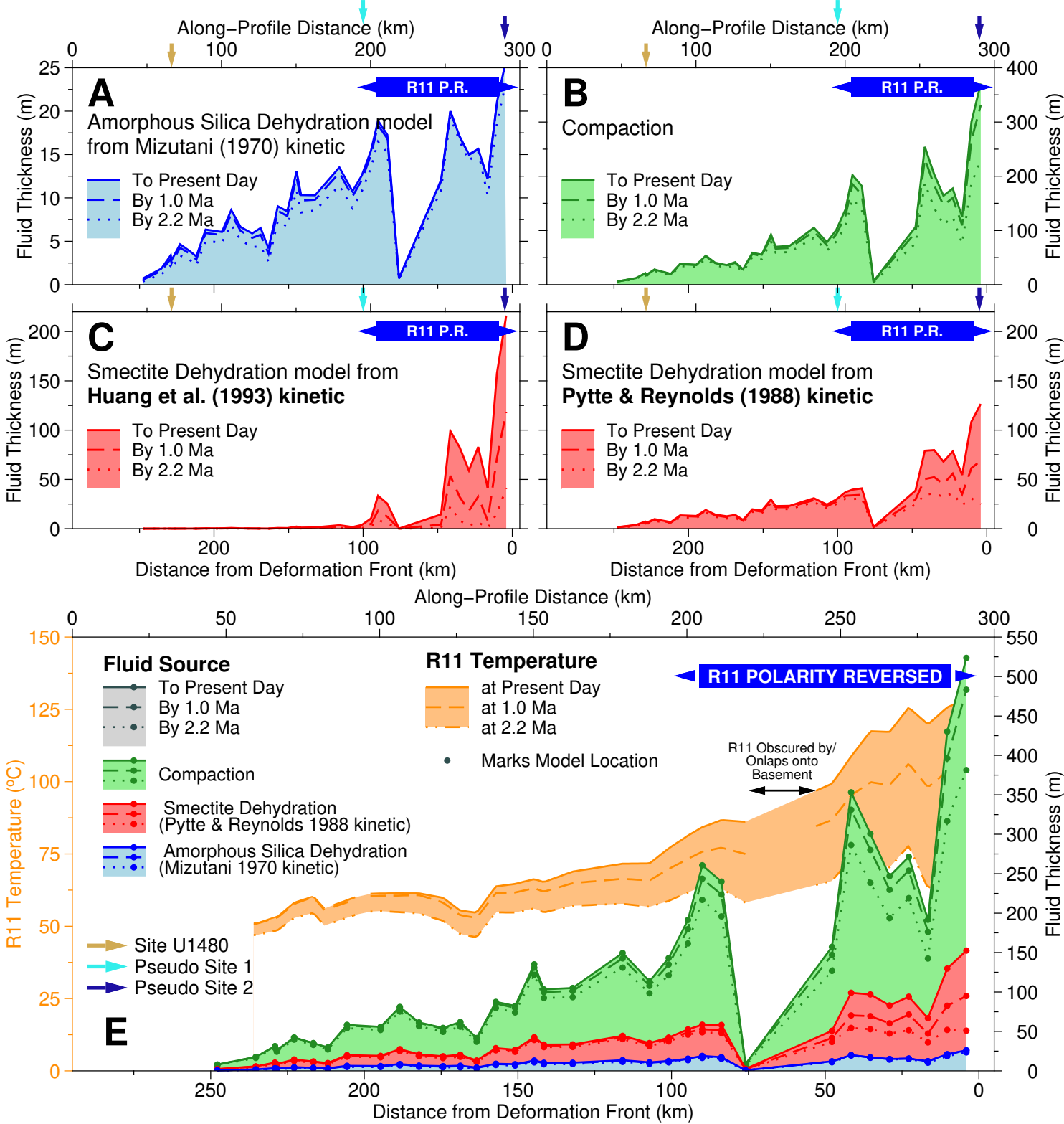
Along–Profile Distance (km)
0
100
200
300
A
Amorphous Silica Dehydration model
from Mizutani (1970) kinetic
To Present Day
By 1.0 Ma
By 2.2 Ma
R11 P.R.
Fluid Thickness (m)
B
Compaction
C
Smectite Dehydration model from
Huang et al. (1993) kinetic
D
Smectite Dehydration model from
Pytte & Reynolds (1988) kinetic
Distance from Deformation Front (km)
E
Fluid Source
Compaction
Smectite Dehydration
(Pytte & Reynolds 1988 kinetic)
Amorphous Silica Dehydration
(Mizutani 1970 kinetic)
R11 Temperature
at Present Day
at 1.0 Ma
at 2.2 Ma
Marks Model Location
R11 POLARITY REVERSED
R11 Obscured by/
Onlaps onto
Basement
Site U1480
Pseudo Site 1
Pseudo Site 2
R11 Temperature (°C)